AD NUMBER
ADB001218
LIMITATION CHANGES

TO:

Approved for public release; distribution is unlimited.

FROM:

Distribution authorized to U.S. Gov't. agencies only; Test and Evaluation; AUG 1974. Other requests shall be referred to Air Force Armament Laboratory, Attn: DLJI, Eglin AFB, FL 32542.

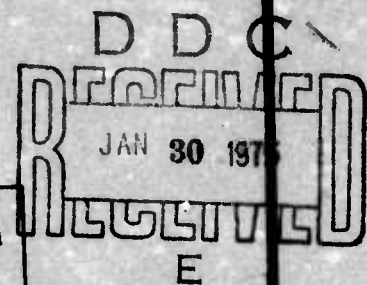| AUTHORITY |
| --- |

afatl ltr, 2 feb 1977

AFATL-TR-74-123

FUNDAMENTAL ASPECTS
OF
UNCONFINED EXPLOSIONS

DEPARTMENT OF AEROSPACE ENGINEERING

THE UNIVERSITY OF MICHIGAN

TECHNICAL REPORT AFATL-TR-74-123

AUGUST 1974

D D C

JAN 30 1975

RECEIVED

E

AIR FORCE ARMAMENT LABORATORY

AIR FORCE SYSTEMS COMMAND • UNITED STATES AIR FORCE

EGLIN AIR FORCE BASE, FLORIDA

AD B001218

Fundamental Aspects
Of
Unconfined Explosions

J.A. Nicholls

M. Sichel

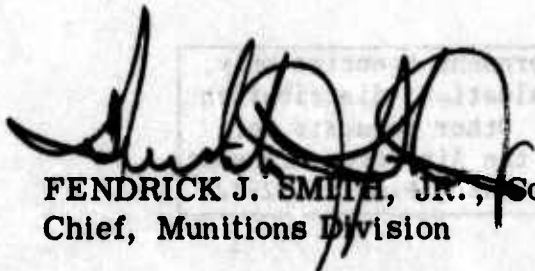R.S. Fry

C. Hu

R. DeSaro

K. Kearney

FOREWORD

This report covers the progress made in the third and final year, 22 January 1973 through 2 February 1974, on a research program conducted by the Department of Aerospace Engineering, The University of Michigan, Ann Arbor, Michigan, under Contract F08635-71-C-0083 with the Air Force Armament Laboratory, Armament Development Test Center, Eglin Air Force Base, Florida. Dr. J.C. Foster, Jr. (DLJI) served as program manager for the Armament Laboratory. Contractor research was directed by Professor J.A. Nicholls.

This technical report has been reviewed and is approved for publication.

FOR THE COMMANDER

FENDRICK J. SMITH, JR., Colonel, USAF
Chief, Munitions Division

ii

ABSTRACT

A simplified version of a combustible cloud is considered wherein the cloud is homogeneous throughout. Blast wave initiation of detonation in this cloud is treated. The self-similar character of strong blast waves and Chapman-Jouguet detonation waves is used to arrive at simplified closed form solutions for the generation of ground impulse and dynamic impulse, up to the time that the detonation arrives at the edge of the cloud. As a result, assessment of the effects of fuel properties and cloud geometry are readily obtained. The influence of side relief at the top of the cloud on the ground impulse is also considered.

Current experimental research is described which investigated the initiation, transition and quasi-steady propagation processes associated with blast initiated, cylindrical detonation waves. Experiments were conducted with gaseous and heterogeneous fuel-air mixtures, using a specially designed sectored shock tube, and the results compared with simplified analytical descriptions. Gas phase detonation research has provided insight into both overall and detailed wave behavior for a full volumetric range of Methyl Acetylene, Propane, Propadiene (MAPP)-air mixtures. Heterogeneous detonation research has allowed examination of gross wave behavior for limited test conditions and additionally provided details as to the time history of drop breakup and ignition when impacted

by strong blast waves. Both of these phases provide evidence to substantiate, in accordance with existing approximate theories, that the strength of the resultant combustion wave generated is dependent upon the blast source energy.

Variations in fuel concentration and blast source energy were found to have a predictable effect upon wave pressure, propagation velocity, detonation limits, ignition threshold energy limits, wave transition radius, and wave transition structure. Comparisons made with the work of others reveal these findings do not suffer from scale effects.

iv

TABLE OF CONTENTS

LIST OF FIGURES

LIST OF FIGURES (concluded)

LIST OF TABLES

LIST OF ABBREVIATIONS, ACRONYMS, AND SYMBOLS

A_f	frontal area of body
a	local acoustic speed
C_D	drag coefficient
C	detonation wave velocity
c_p	specific heat at constant pressure
D_o	initial drop diameter
E	energy release
E_o	total instantaneous energy release per unit area or per unit length respectively for planar or cylindrical blast wave geometry
$E_{M_{CJ}}$	blast wave source energy at the experimentally established condition of $M = M_{CJ}$
$E_{M_{max}}$	blast wave source energy at the experimentally established condition of $M = M_{maximum}$
F_d	aerodynamic force on body
h	height of cloud
I	normalized impulse, Eq. (8)
$\bar{I}$	total impulse imparted to ground
$\bar{I}_b$	ground impulse from blast wave
$\bar{I}_d$	ground impulse from detonation
$\bar{I}_v$	dynamic impulse
$\mathcal{L}$	dimensionless impulse
$\mathcal{I}$	impulse per unit area at distance r

LIST OF ABBREVIATIONS, ACRONYMS, AND SYMBOLS (continued)

L	length
M	Mach number
M_{s_i}	Mach number at condition of interaction between shock and fuel drop
$M_{R=24\ in.}$	Mach number in ..ectored chamber at radial distance of $R = 24$ in. referenced from hypothetical origin
$\mathcal{M}_i$	molecular weight
P	dimensionless pressure
P_b	universal pressure function
p	pressure
Q	heat release per unit mass of mixture due to chemical reaction
$\widehat{Q}$	dimensionless heat release
q	dynamic pressure
q_i	drop dynamic pressure at shock/drop incidence, $1/2\ \rho_i\ u_1^2$
q_b	drop dynamic pressure at local breakup condition, $1/2\ \rho_2\ u_2^2$
R	dimensionless density, or radius
R	universal gas constant
Re_i	drop Reynolds number at shock/drop incidence, $\rho_1\ u_1\ D_0/\mu_1$
Re_b	drop Reynolds number at local breakup conditions, $\rho_2\ u_2\ D_0/\mu_1$
r	linear spatial coordinate-radius
r_0	explosion length

T	temperature
T	dimensional time
$\bar{t}$	dimensionless time, $u_2 \, (\rho_2/\rho_f)^{1/2} \, t/D_o$
$\tilde{t}$	reduced time, t/D_o
t_n	initial period of side relief
U	universal impulse function
U_v	universal dynamic impulse function
u	fluid velocity
V	dimensionless fluid velocity
v	fluid velocity
We_i	drop Weber number at shock/drop incidence, $\rho_1 \, u_1^2 \, D_o/\sigma_f$
We_b	drop Weber number at local breakup conditions, $\rho_2 \, u_2^2 \, D_o/\sigma_f$
x	distance
x	distance from wave front
$\bar{x}$	dimensionless distance
z	ratio of dimensionless pressure to dimensionless density
α	blast wave parameter
α	regression coefficient
β	blast wave impulse function
β	regression coefficient

LIST OF ABBREVIATIONS, ACRONYMS, AND SYMBOLS (continued)

γ	ratio of specific heats
Δ	reaction zone thickness
δ	detonation impulse function
δ	turning angle
θ	shock wave angle
λ	dimensionless independent similarity variable
μ	viscosity
ν	geometric constant equal to 1, 2, or 3 for plane, cylindrical, or spherical cloud geometry
ξ	dimensionless distance
ρ	density
σ	surface tension
σ_ν	geometric cloud factor
τ	dimensionless time, t/t_s
τ_t	initial transient period
ϕ	equivalence ratio

Subscripts

1	static
1	upstream of incident shock
2	downstream of incident shock
3	downstream of C-J plane

LIST OF ABBREVIATIONS, ACRONYMS, AND SYMBOLS (concluded)

b	blast wave
b	drop breakup
CJ	Chapman-Jouguet
crit	critical
d	detonation
e	explosive
f	fuel
g	gas
i	inert
i	shock/drop incident
ig	drop ignition
s	shock or wave
s	spherical detonation
st	drop stripping
th	theoretical
*	critical

SECTION I

INTRODUCTION

Many facets of unconfined explosions, such as a fuel-air explosion, are ill understood. Theoretical treatments as well as carefully controlled experimental studies of the problem have been relatively few. The aim of this research program is to add to the understanding through an integrated analytical and experimental study. The idea has been to treat a simplified model of the explosive cloud so that general conclusions can be drawn. For example, it is desirable to understand the pressure and velocity fields that are set up, the impulse characteristics, the influence of fuel properties, the influence of cloud geometry and non-uniform distribution of fuel throughout the cloud, the detonation initiation requirements, etc. Many of these subjects, but not all, are treated in this report. The theoretical aspects are taken up in Section II and the results of experimental studies are discussed in Section III.

1

SECTION II

THE IMPULSE GENERATED BY BLAST WAVES PROPAGATING
THROUGH COMBUSTIBLE MIXTURES

A. INTRODUCTION

Detonations can be initiated in combustible mixtures by sufficiently strong blast waves. Such blast initiated detonations, or fuel-air explosions, are of interest in certain military applications, and may also arise in industrial accidents. The ground and dynamic impulse generated by such explosions is a main cause of damage; hence, it is important to determine the influence of the fuel properties, the cloud geometry, and the size of the initiating charge upon the impulse which is generated. The analytical determination of the impulse generated by a fuel-air explosion forms the subject of the present paper.

The shape of the fuel cloud and the fuel distribution, which will have important effects upon the ground impulse, will generally be quite complex, depending on the method of fuel dispersal. Analytical determination of ground impulse therefore is possible only if simplified models of fuel-air explosions are used. Use of appropriately formulated models makes it possible to rapidly estimate the effects of the fuel properties and cloud geometry upon the impulse and also provides a basis of assessing experimental data from fuel-cloud explosions.

2

Hence, it is assumed that fuel is distributed uniformly through the cloud with Q, the combustion energy released per unit mass of fuel-oxidizer mixture. Clouds with planar, cylindrical and spherical symmetry are considered. It is known[1,2,3,4] that the initiating blast wave is dominant at first but that later the explosion consists of a Chapman-Jouguet detonation propagating through the fuel-cloud. The transition between blast wave and detonation behavior occurs near a critical radius r_* within which the total combustion energy release equals the energy E_o of the initiating blast wave. This condition leads to the relation

$$r_* = (\nu E_o / \sigma_\nu Q \rho_1)^{1/\nu} \tag{1}$$

where $\nu = 1, 2, 3$ and $\sigma_\nu = 2, 2\pi, 4\pi$ for planar, cylindrical, and spherical symmetry. The flow in the transition region when the explosion radius r_s is of the order of r_* is very complicated. However, it is shown by Nicholls et al.[1] that a zeroth order model in which self-similar blast wave and detonation wave theory are used for $r_s < r_*$ and $r_s > r_*$ respectively, yields analytical results in reasonable agreement with experiments carried out in a special pie-shaped shock tube, designed to simulate an explosion with cylindrical symmetry.

This zeroth order model also is the basis of the impulse calculations described below, and leads to results which permit rapid

3

computation of the impulse using universal impulse functions. In the planar and cylindrical cases it is at first assumed that the fuel-cloud extends from the ground plane to an infinite height or, what is equivalent, that the explosion is confined by a non-yielding plane which is parallel to the ground. With this model the influence of the fuel used, the fuel-oxidizer mixture ratio, and the blast energy upon the impulse generated by the wave is readily determined. The total ground impulse and the static dynamic impulse at a fixed distance from blast center generated by the explosions of such confined clouds are considered in Parts B through G.

Actually, of course, the upper surface of the fuel-clouds is bounded by inert air or oxidizer rather than by a non-yielding surface. Thus, as the detonation propagates through the cloud an expansion wave will eat into the high pressure combustion products behind the wave. This side relief will cause considerable reduction in the ground impulse generated by the wave and will depend, mainly, on the height of the fuel-cloud. Simplified models for estimating this effect are considered in Part H.

B.   THE TOTAL GROUND IMPULSE

The pressure p, within the leading shock of a FAE (fuel-air explosion), i.e., in the region $r < r_s$, will be a function of the radial distance r from the blast center. If p_1 is the ambient pressure ahead

4

of the wave, then the ground impulse generated by the FAE per unit area at a given point during the time interval dt is $(p - p_1) dt$. The total impulse $d\bar{I}$ generated in the region $r < r_s$ during dt is then given by

$$d\bar{I} = \left\{ \int_0^{r_s(t)} \left[p(r,t) - p_1 \right] \sigma_\nu \, r^{\nu-1} \, dr \right\} dt \qquad (2)$$

The index $\nu = 1$ for planar waves but $\nu = 2$ for both cylindrical and spherical waves since each exerts pressure on a circular area. Fuel-air explosions with planar, cylindrical and spherical symmetry are shown in Figure 1. The total ground impulse $\bar{I}(t)$ at time t after initiation of the secondary blast will then be

$$\bar{I}(t) = \sigma_\nu \int_0^t \int_0^{r_s(t)} \left[p(r,t) - p_1 \right] r^{\nu-1} \, dr \, dt \qquad (3)$$

It is important to recognize that in the planar case $\bar{I}(t)$ is the impulse applied to a strip of unit width.

In general, evaluation of the impulse from Equation (3) will require extensive numerical integration. The integral (3) can, however, be greatly simplified for the self-similar blast waves and detonation waves which are used in the zeroth order FAE model described in Part A.

5
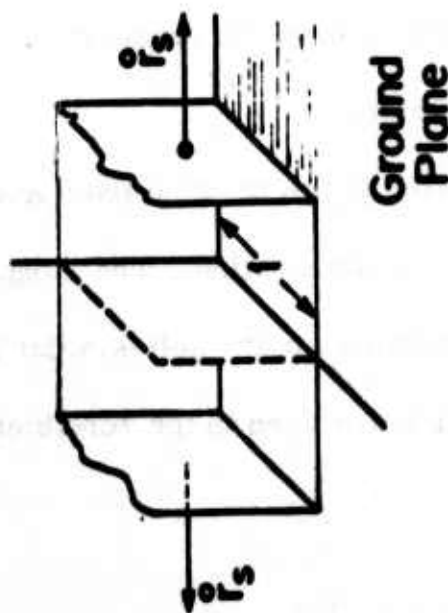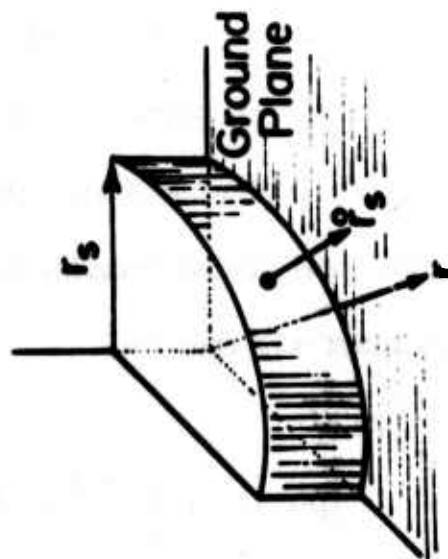
Planar Wave   **Cylindrical Wave**   **Spherical Wave**
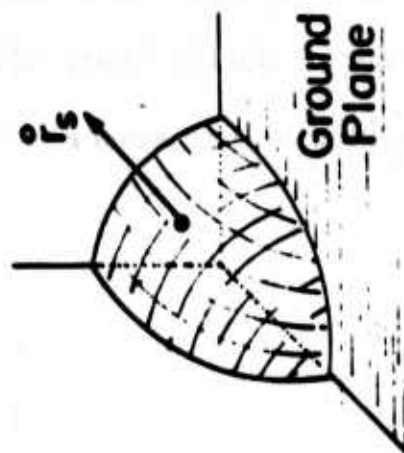
Figure 1. Fuel-Air Explosions with Planar, Cylindrical and Spherical Symmetry.

6

C. BLAST WAVE IMPULSE

When $r < r_*$ the FAE is thus replaced by a strong blast wave. The self-similar solution for a strong blast wave is discussed in detail by Sedov[5] and Taylor[6]. The key assumptions are that the shock pressure ratio $(p_2/p_1) \gg 1$, that the release of explosive energy, E_0, is instantaneous, and that the fluid is a perfect gas, with constant specific heats. Then it can be shown that the shock radius r_s, and the fluid velocity v_2, pressure p_2, and temperature T_2 immediately behind the shock front are given by

$$r_s = \left(\frac{E_0}{\alpha \rho_1}\right)^{1/\nu+2} t^{2/\nu+2}$$

$$v_2 = \frac{4}{(\nu+2)(\gamma+1)} \left(\frac{E_0}{\alpha \rho_1}\right)^{1/\nu+2} t^{-\nu/\nu+2}$$

$$p_2 = \frac{8\rho_1}{(\nu+2)^2 (\gamma+1)} \left(\frac{E_0}{\alpha \rho_1}\right)^{2/\nu+2} t^{-2\nu/\nu+2}$$ (4)

$$T_2 = \frac{8(\gamma-1)}{(\nu+2)^2 (\gamma+1)^2} \left(\frac{E_0}{\alpha \rho_1}\right)^{2/\nu+2} t^{-2\nu/\nu+2}$$

E_0 is the blast energy released instantaneously per unit area, length, or at a point for $\nu = 1, 2, 3$. The function $\alpha(\gamma, \nu)$, which is derived from the requirement that the total energy for $r < r_s$ must equal E_0 is shown in Figure 2. The dimensionless pressure

7
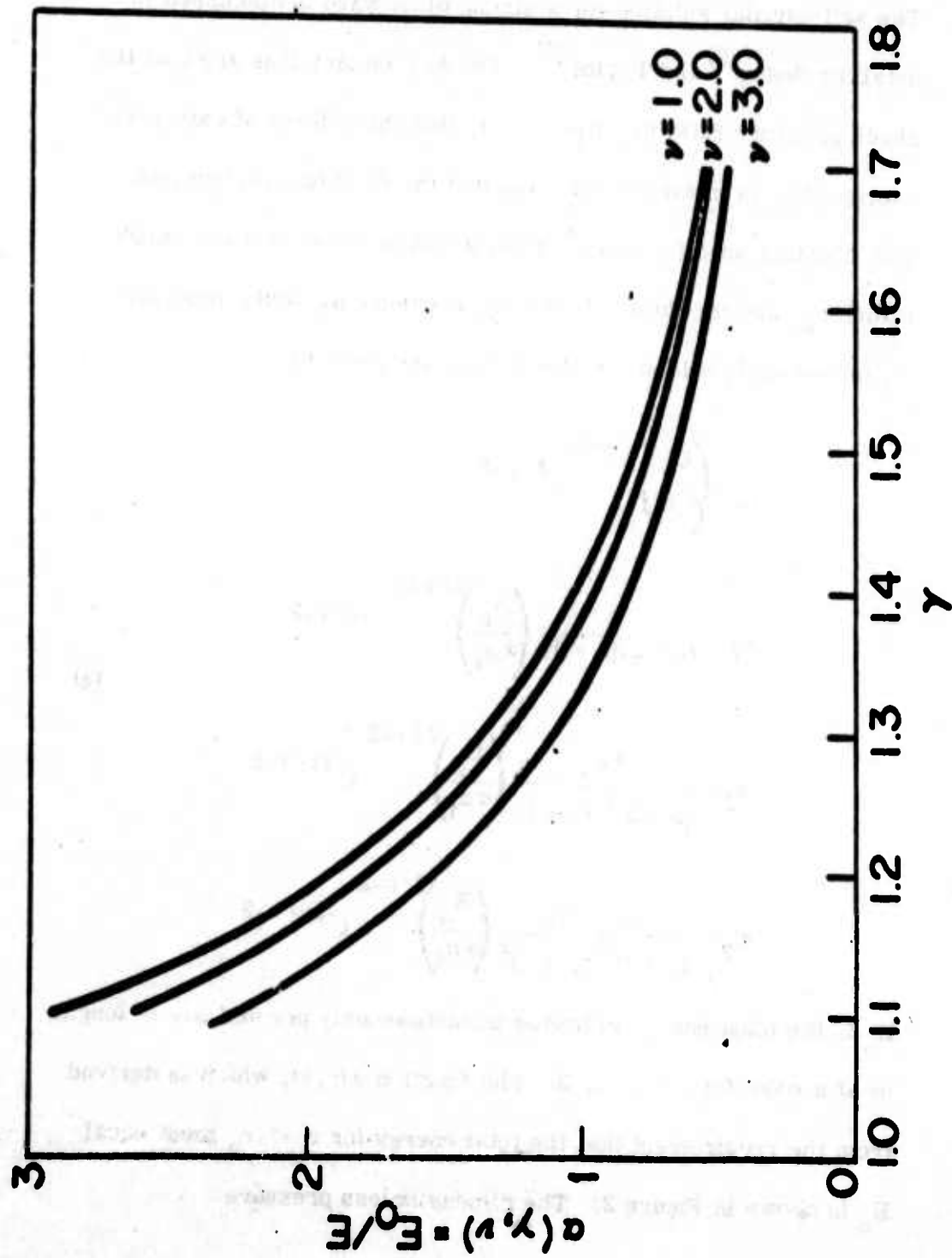
Figure 2. Variation of the Blast Wave Parameter $\alpha(\gamma, \nu)$ with γ.

$$P_b(\lambda, \nu) = p/\rho_1 \left(\frac{r^2}{t^2}\right) = \left(\frac{p}{p_2}\right) \frac{8}{(\nu + 2)^2 \, (\gamma + 1)} \frac{1}{\lambda^2} \tag{5}$$

is a function of only the normalized radius $\lambda = r/r_s$, the geometric index ν, and the ratio of specific heats γ.

Neglecting p_1, and introducing Equations (4) and (5) in Equations (3) reduces the impulse integral to the form

$$\overline{I}_b(t) = \sigma_\nu \, E_o \frac{\beta(\gamma, \nu)}{\alpha(\gamma, \nu)} t \quad ; \quad \nu = 1, 2$$

$$\tag{6}$$

with

$$\beta(\gamma, \nu) = \int_0^1 P_b(\lambda, \nu) \lambda^{\nu+1} \, d\lambda$$

The integral $\beta(\gamma, \nu)$ depends only on the ratio of specific heats γ and the geometric index ν, and can be evaluated from the self-similar blast wave solution which is presented in analytical form by Sedov[5]. For spherical blast waves, which act on a circular area, the total impulse is given by

$$\overline{I}_b(t) = \frac{10}{3} \pi \, \rho_1 (E_o/\alpha \rho_1)^{4/5} \beta(\gamma, 3) \, t^{3/5}$$

with

$$\tag{7}$$

$$\beta(\gamma, 3) = \int_0^1 P_b(\lambda, 3) \lambda^3 \, d\lambda$$

9

The functions $\beta(\gamma, \nu)$ for $\nu = 1, 2, 3$, are plotted in Figure 3. The impulse from planar and cylindrical waves increases more rapidly with time than for a spherical wave. This result is to be expected since the spherical geometry provides more pressure relief than the confined planar and cylindrical geometry.

Equations (6) and (7) also suggest the introduction of a normalized impulse I defined by

$$I_b = \bar{I}_b(t)/E_o t = \sigma_\nu \frac{\beta(\gamma, \nu)}{\alpha(\gamma, \nu)} \quad ; \quad \nu = 1, 2$$

$$I_b = \bar{I}_b(t)/\rho_1(E_o/\rho_1)^{4/5} t^{3/5} = \frac{10\pi}{3} \frac{\beta(\gamma, 3)}{[\alpha(\gamma, 3)]^{4/5}} \quad ; \quad \nu = 3$$

$$(8)$$

The variation of the normalized impulse I with the ratio of specific heats γ is shown in Figure 4. Using Equation (4) the time t in the expressions for $\bar{I}(t)$ can be replaced by the shock radius so that

$$\bar{I}_b(r_s) = \sigma_\nu(E_o \rho_1/\alpha)^{1/2} \beta r_s^{\frac{\nu+2}{2}} \quad ; \quad \nu = 1, 2$$

$$\bar{I}_b(r_s) = \frac{10}{3}\pi (E_o/\rho_1/\alpha)^{1/2} \beta r_s^{3/2} \quad ; \quad \nu = 3$$

$$(9)$$

D. DETONATION WAVE IMPULSE

When $r_s > r_*$, the self-similar solution for the flow behind a Chapman-Jouguet (CJ) detonation[5] is used to represent the FAE. The total ground impulse generated by a CJ detonation is also given

10
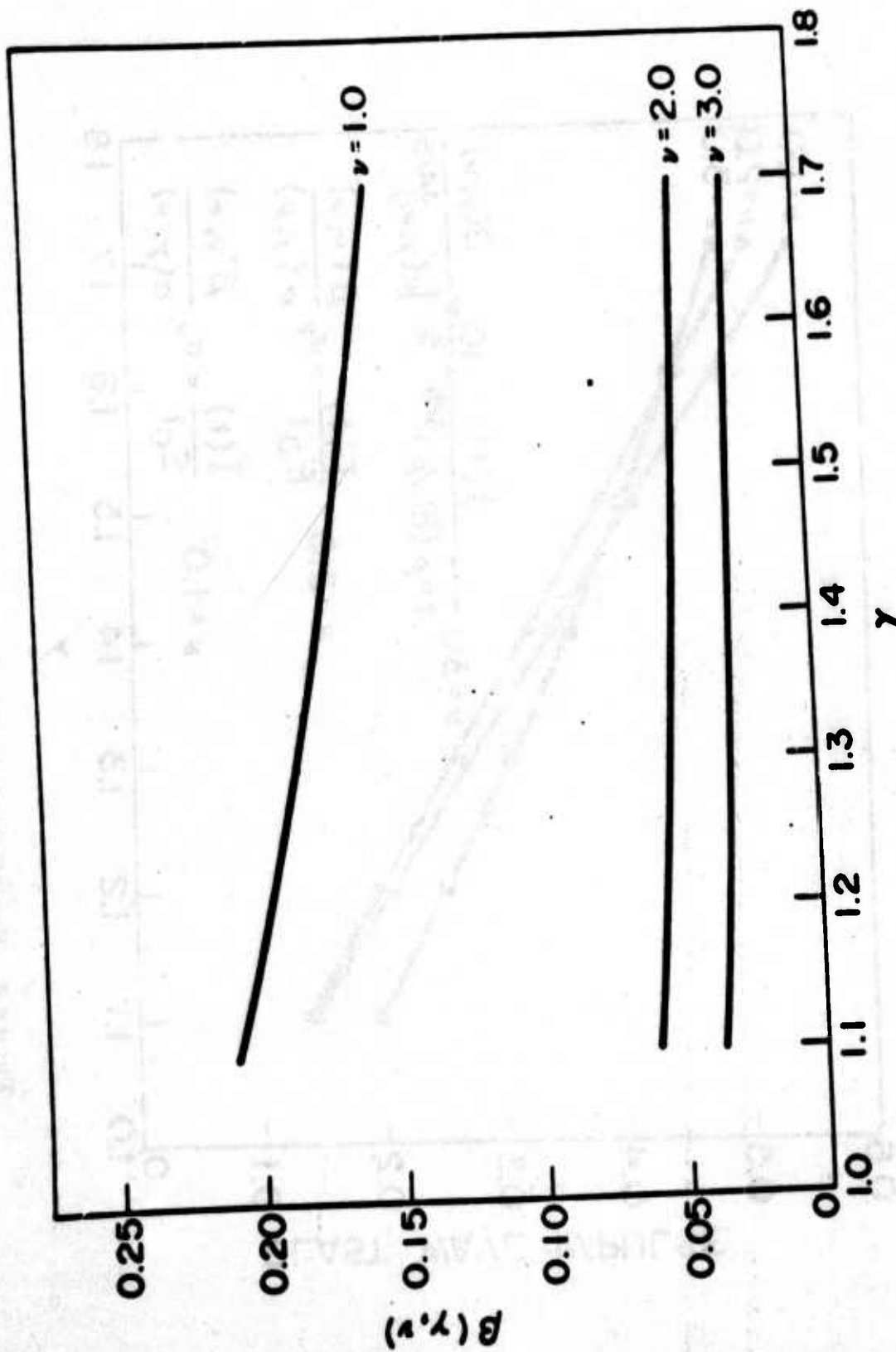
Figure 3. Variation of the Blast Wave Impulse Function $\beta(\gamma, \nu)$ with ν and γ.

11
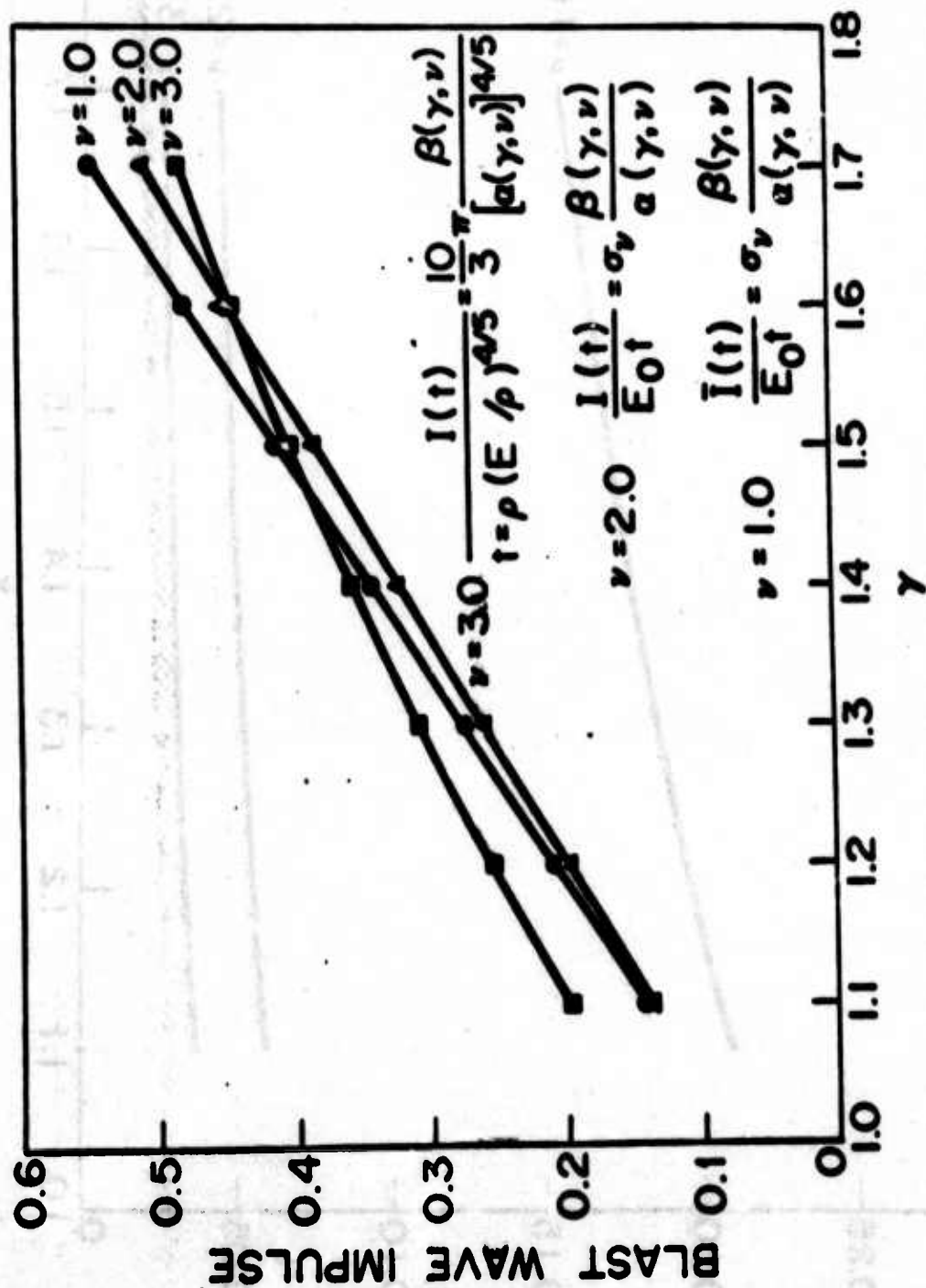
Figure 4. Variation of the Normalized Blast Wave Impulse.

by Equation (3); however, the ambient pressure p_1 is no longer negligible compared to the pressure p_2 behind the detonation front. As before, a dimensionless pressure P_d defined by

$$P_d(\lambda, \nu) = p/\rho_1 \left(\frac{r^2}{t^2}\right) \tag{10}$$

is introduced. In contrast to the strong blast wave, a detonation front propagates with a constant velocity C so that

$$r_s = Ct \tag{11}$$

Precise determination of the pressure ratio, temperature ratio, density ratio and propagation speed of CJ detonations requires the determination of the equilibrium composition of the products of combustion, and has been carried out numerically using the computer code of Gordon and McBride[7]. Detonation parameters for methane-air and MAPP gas-air mixtures computed with this code are shown in Figures 5 and 6 and are typical of hydrocarbon-air detonations. Once the propagation velocity C, detonation Mach number M_d, the ratios of specific heats γ_1, and γ_2, and the molecular weight $\mathcal{M}_2$, of the combustion products have been determined numerically, other detonation properties can be determined from the perfect gas Hugoniot Equations with remarkable accuracy. The equations for mass, momentum, and energy conservation across

13

ρ_1 (slug/ft^3)

0.00330
0.00225
0.00220
0.00215
0.00210
0.00205

C

m_1

m_2

ρ_1

ϕ

0.4 0.6 0.8 1.0 1.2 1.4 1.6 1.8 2.0 2.2

m_1, m_2 (mol wt)

29
28
27
26
25
24
23
22
21

m_1, m_2 (mol wt)

C (ft/sec)

6200
6000
5800
5600
5400
5200
5000
4800
4600
4400

C (ft/sec)
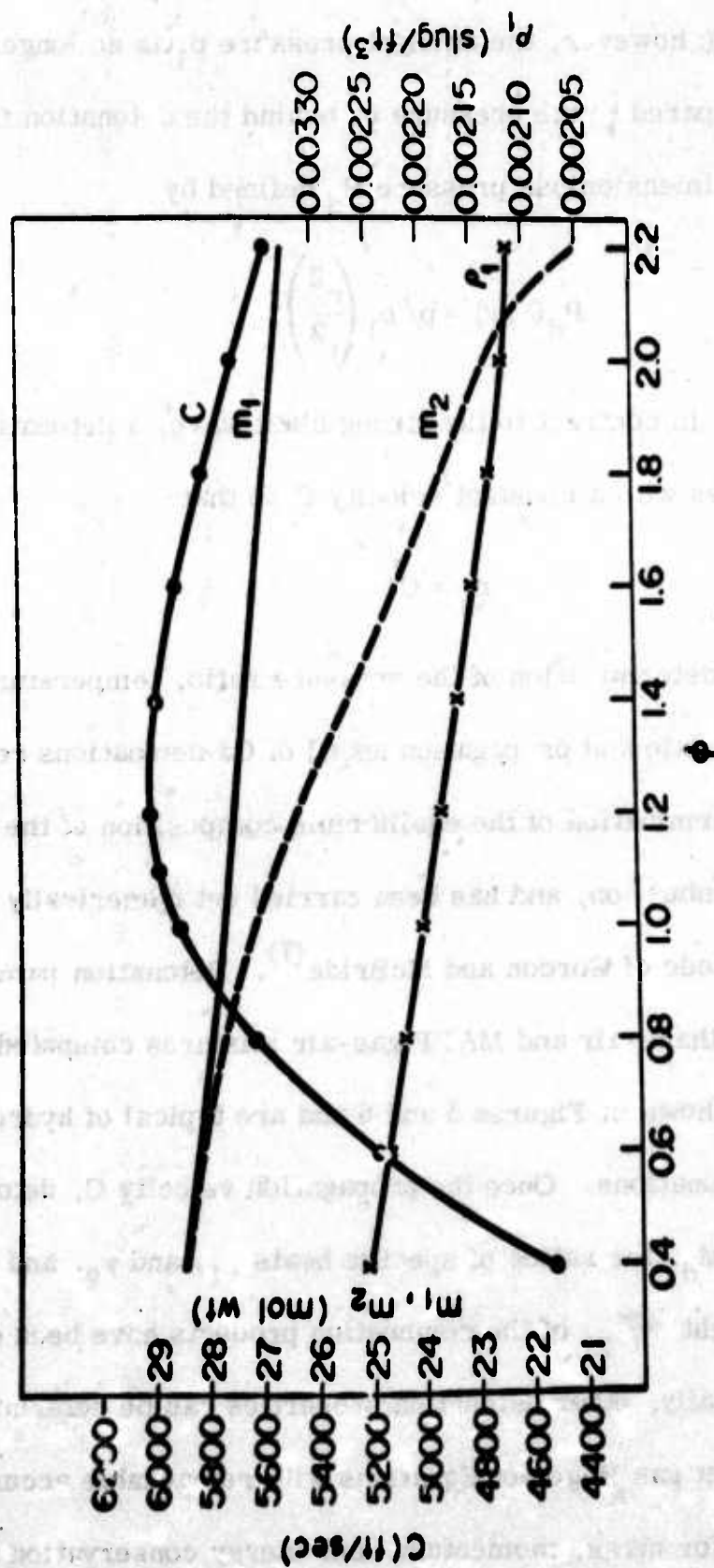
Figure 5a. Detonation Properties for Methane-Air Mixtures.

14
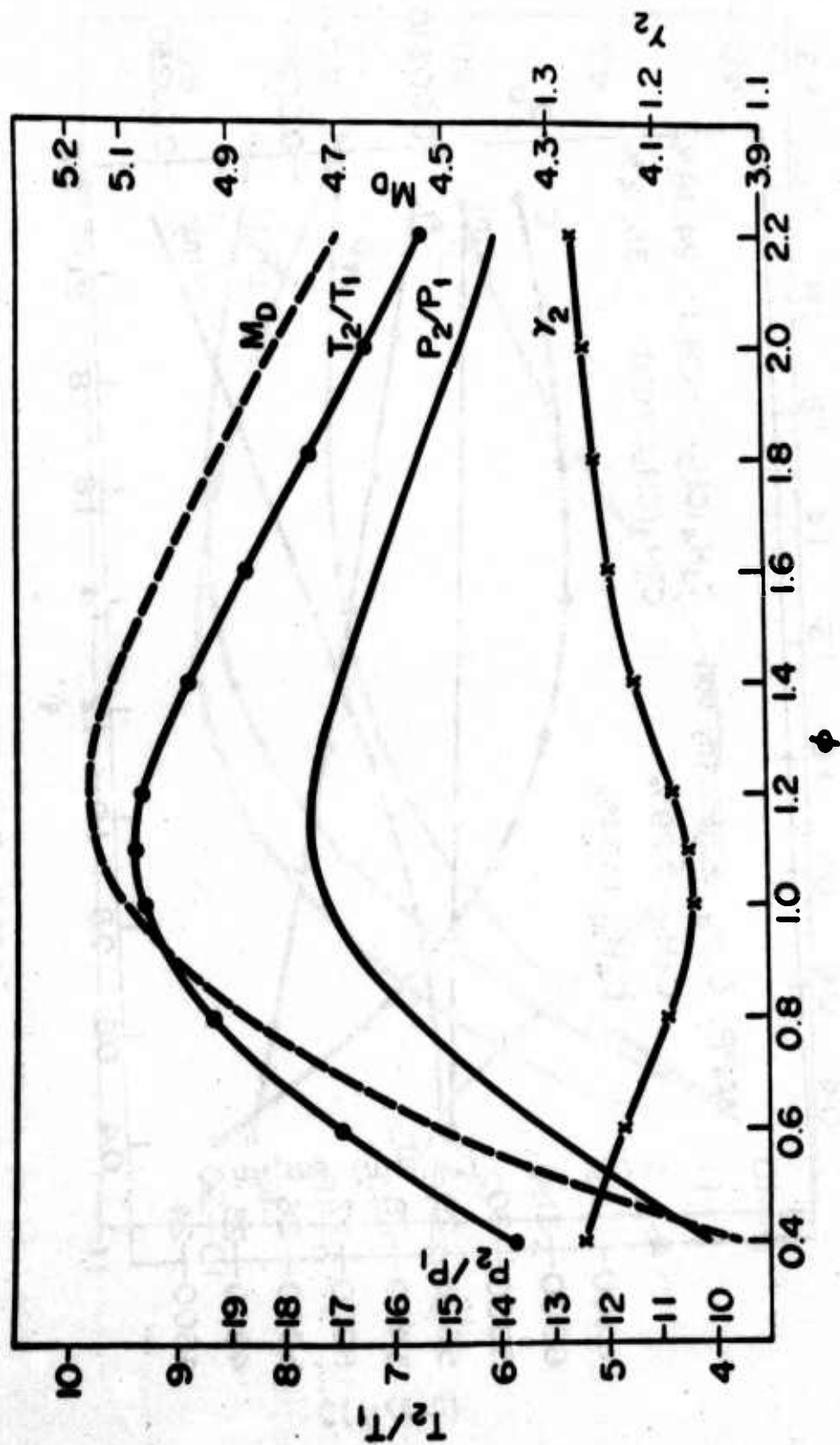
Figure 5b. Detonation Properties for Methane-Air Mixtures.
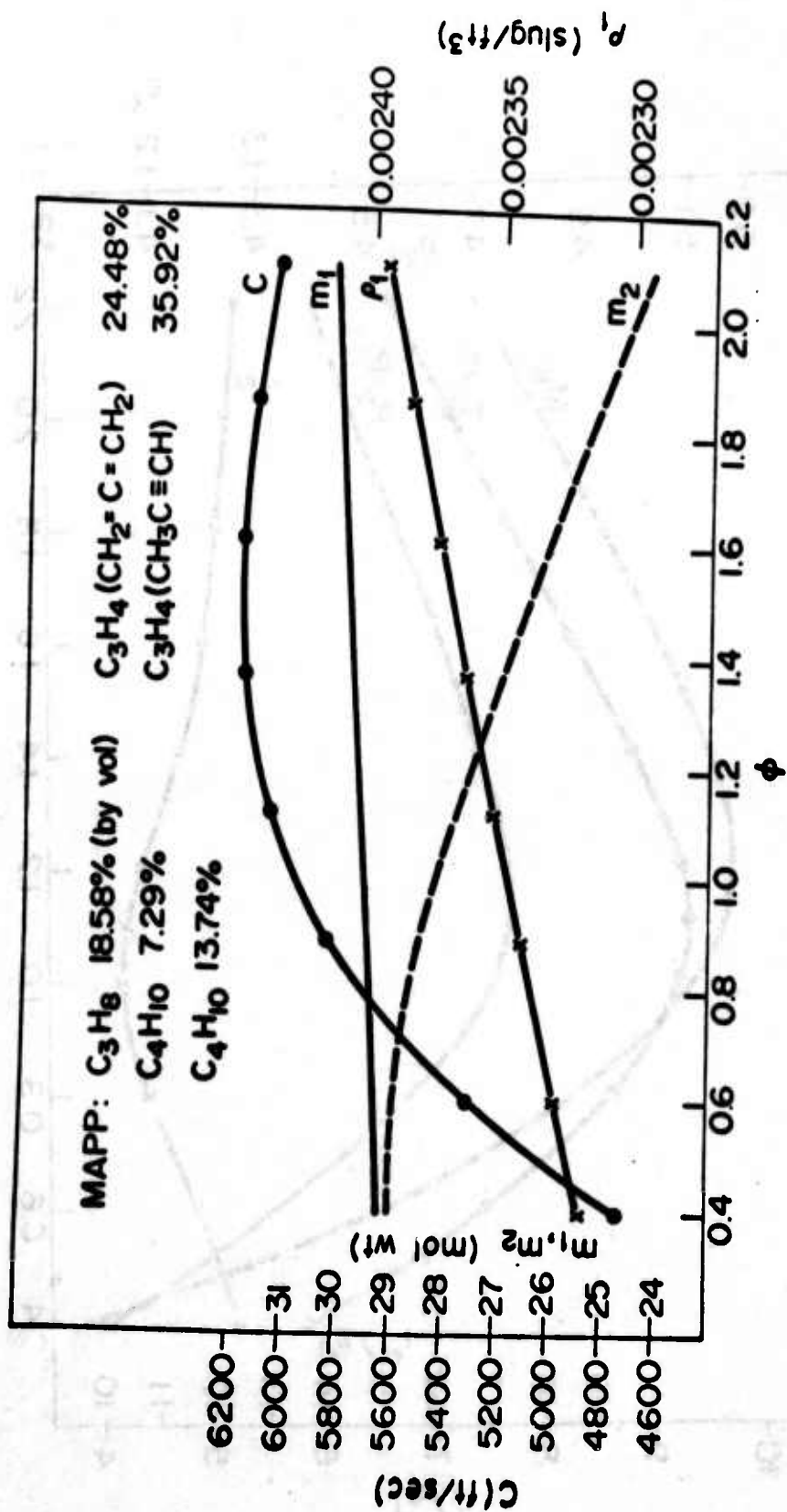
Figure 6a. Detonation Properties for MAPP-Air Mixtures.

16
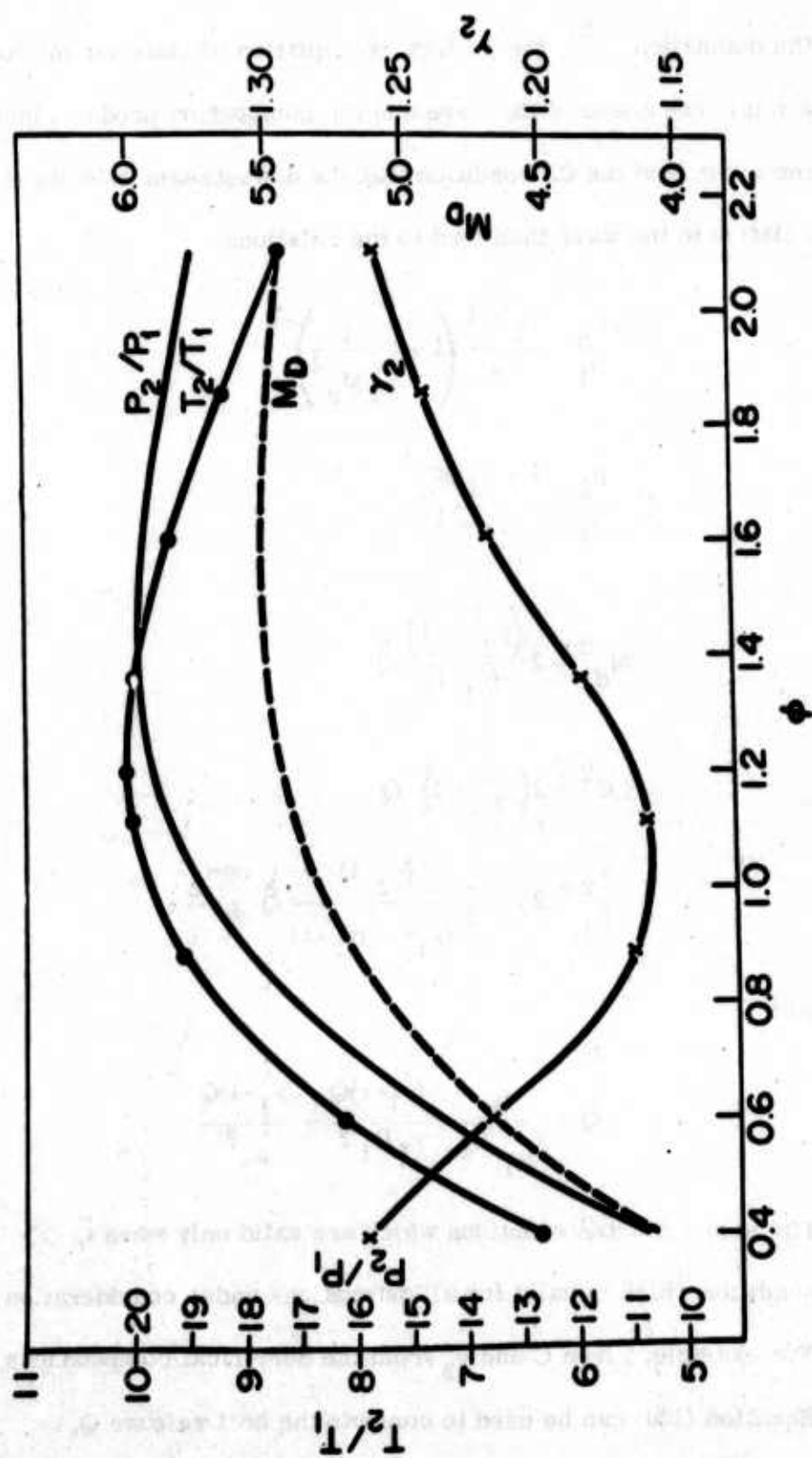
Figure 6b. Detonation Properties for MAPP-Air Mixtures.

the detonation[5, 8], the perfect gas equation of state for the fuel-air mixture ahead of the wave and the combustion products behind the wave, and the CJ condition that the downstream velocity is sonic relative to the wave then lead to the relations:

$$\frac{\rho_2}{\rho_1} = \frac{\gamma_2 + 1}{\gamma_2}\left(1 + \frac{1}{\gamma_1 M_d^2}\right)^{-1} \tag{12a}$$

$$\frac{p_2}{p_1} = \frac{1 + \gamma_1 M_d^2}{\gamma_2 + 1} \tag{12b}$$

$$M_d^2 \cong 2\frac{\left(\gamma_2^2 - 1\right)}{(\gamma_1 - 1)}\hat{Q} \tag{12c}$$

$$C^2 \cong 2\left(\gamma_2^2 - 1\right)Q \tag{12d}$$

$$\frac{T_2}{T_1} \cong 2\gamma_1\gamma_2\frac{(\gamma_2 - 1)}{(\gamma_1 - 1)(\gamma_2 + 1)}\hat{Q}\frac{\mathscr{M}_2}{\mathscr{M}_1} \tag{12e}$$

with

$$\hat{Q} = \frac{Q}{c_{p_1} T_1} = \frac{(\gamma_1 - 1)Q}{\gamma_1 R_1 T} = \frac{(\gamma_1 - 1)Q}{a_1^2}$$

The sign $\cong$ denotes equations which are valid only when $\hat{Q} \gg 1$, a condition which is valid for all detonations under consideration here. For example, given C and γ_2 from the numerical computations, Equation (12d) can be used to compute the heat release Q,

18

which also occurs in the expression (1) for critical radius r_*.

Introduction of Equations (10), (11), and the similarity variable $\lambda = r/r_s$ into the equation for the total impulse yields the result

$$\bar{I}_d(t) = \frac{\sigma_\nu \rho_1 C^{\nu+2} t^{\nu+1}}{\nu+1} \left[\delta(\gamma_2, \nu) - \frac{1}{\nu \gamma_1 M_d^2} \right] \quad ; \quad \nu = 1, 2$$

$$\bar{I}_d(t) = \frac{2\pi \rho_1 C^4 t^3}{3} \left[\delta(\gamma_2, 3) - \frac{1}{2\gamma_1 M_d^2} \right] \quad ; \quad \nu = 3$$

(13)

where

$$\delta(\gamma_2, \nu) = \int_0^1 P_d(\lambda, \nu) \lambda^{\nu+1} \, d\lambda \quad ; \quad \nu = 1, 2$$

$$\delta(\gamma_2, 3) = \int_0^1 P_d(\lambda, 3) \lambda^3 \, d\lambda \quad ; \quad \nu = 3$$

(14)

Using Equation (11) the impulse $\bar{I}_d$ can also be expressed in terms of the detonation radius r_s with the result

$$\bar{I}_d(r_s) = \frac{\sigma_\nu \rho_1 C r_s^{\nu+1}}{\nu+1} \left[\delta(\gamma_2, \nu) - \frac{1}{\nu \gamma_1 M_d^2} \right] \quad ; \quad \nu = 1, 2$$

$$\bar{I}_d(r_s) = \frac{2\pi \rho_1 C r_s^3}{3} \left[\delta(\gamma_2, 3) - \frac{1}{2\gamma_1 M_d^2} \right] \quad ; \quad \nu = 3$$

(15)

The variation of $P_d(\lambda, \nu)$, and hence the self-similar solution for the flow behind a CJ detonation must be known to compute the integrals $\delta(\gamma_2, \nu)$. This self-similar solution cannot be found in analytical form, and as indicated by Sedov[5] the key step is integration of the non-linear differential equation

$$\frac{dz}{dv} = \frac{z[\,2(V-1)^2 + (\nu - 1)(\gamma_2 - 1)\,V(V-1) - 2z]}{V[\,(V-1)^2 - \nu z]} \tag{16}$$

The dimensionless velocity $V(\lambda)$ and the variables $z(\lambda)$ are defined by

$$V(\lambda) = \frac{V}{(r/t)} \quad ; \quad z = \gamma_2 \frac{P_d(\lambda)}{R_d(\lambda)} \quad ; \quad R_d(\lambda) = \frac{\rho}{\rho_1} \tag{17}$$

Integration of Equation (16) must be carried out numerically and starts at the point

$$z_2 = \frac{\gamma_2^2}{(\gamma_2 + 1)^2} \left(1 + \frac{1}{\gamma_1 M_d^2}\right)^2 \quad ; \quad V_2 = 1 - \sqrt{z_2} \tag{18}$$

immediately downstream of the detonation front. The solution $z(V)$ thus depends on both γ_2 and the detonation Mach number M_d; however, since $M_d^2 \gg 1$, this latter dependence is very weak. The detonation front is followed by an isentropic expansion through which the velocity of the combustion products decreases to zero at the boundary of a stationary core region corresponding to the point $V = 0$, $z = 1$, a

20

singular point of Equation (16). Details of the numerical solution of Equation (16) are described in Reference 9. All other parameters of the flow behind the detonation are readily determined once the variation of z with V is known[5,9]. Typical velocity, pressure, and temperature profiles behind a CJ detonation are shown in Figure 7.

The function $\delta(\gamma_2, \nu)$ has been calculated for both air-methane and air-MAPP mixtures. For the two fuels considered, γ_2 ranges between 1.16 and 1.31 while M_d lies between 4.0 and 5.0, and over this range $\delta(\gamma_2, \nu)$ is almost independent of γ_2 and the fuel-oxidizer mixture ratio. In fact, $\delta(\gamma_2, \nu)$ depends only on ν for methane and MAPP, and the average value of $\delta(\gamma_2, \nu)$ is given in Table I below. The values of γ_2 and M_d for MAPP and methane are typical of most hydrocarbon-air detonations; hence, the values of $\delta(\gamma_2, \nu)$ in Table I can be used to compute the impulse for hydrocarbon-air CJ detonations in general with reasonable accuracy.

TABLE I. AVERAGE VALUE OF $\delta(\gamma_2, \nu)$

ν	$\delta(\gamma_2, \nu)_{avg}$
1	0.190
2	0.138
3	0.135

Air-Mapp C-J Detonation $\gamma_1 = 1.4$ $\gamma_2 = 1.259$ $M_i = 4.2478$
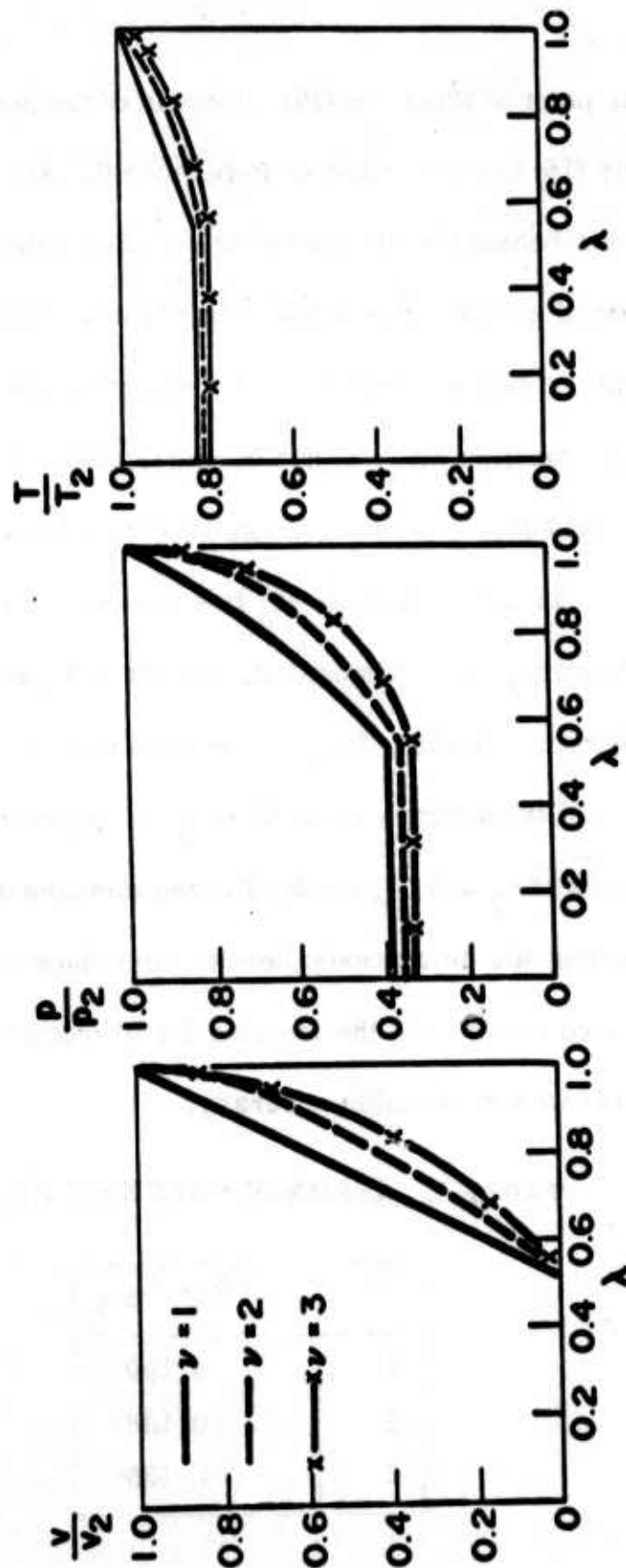
Figure 7. Typical Velocity, Pressure, and Temperature Profiles Behind a CJ Detonation.

The quantities $\bar{I}_d(t)/t^{\nu+1}$ for $\nu = 1, 2$, and $\bar{I}_d(t)/t^3$ for $\nu = 3$ depend on ρ_1, C, and M_d (Equation 13) and so vary appreciably with the type of fuel and with the equivalence ratio ϕ. With these impulse functions, which are plotted for methane-air and MAPP-air mixtures in Figures 8 and 9, $\bar{I}_d(t)$ is readily determined as a function of ϕ. The functions $\bar{I}_d(t)/t^{\nu+1}$, $\bar{I}_d(t)/t^3$, also provide a basis for determining the influence of the fuel composition and mixture ratio upon the total ground impulse. From Figures 8 and 9, for instance, it can be seen that MAPP-air mixtures provide a somewhat higher impulse than methane-air. It is also of interest that the peak impulse occurs for rich mixtures with $\phi = 1.2$ and $\phi = 1.5$ for methane-air and MAPP-air, respectively.

E.   GROUND IMPULSE OF FAE

Both the blast wave and the CJ detonation results must be used to determine the total ground impulse $\bar{I}$ of a FAE. When $r_s < r_*$, $\bar{I}$ is given by

$$\bar{I}(r_s) = \bar{I}_b(r_s) \tag{19}$$

for the zeroth order FAE model described in the Introduction. The blast wave and CJ solutions are patched together when $r_s = r_*$. This means that the entire flow field corresponds to that of a blast wave when $r_s < r_*$, and to that of a CJ detonation when $r_s > r_*$. Accordingly the ground impulse is approximated by

23
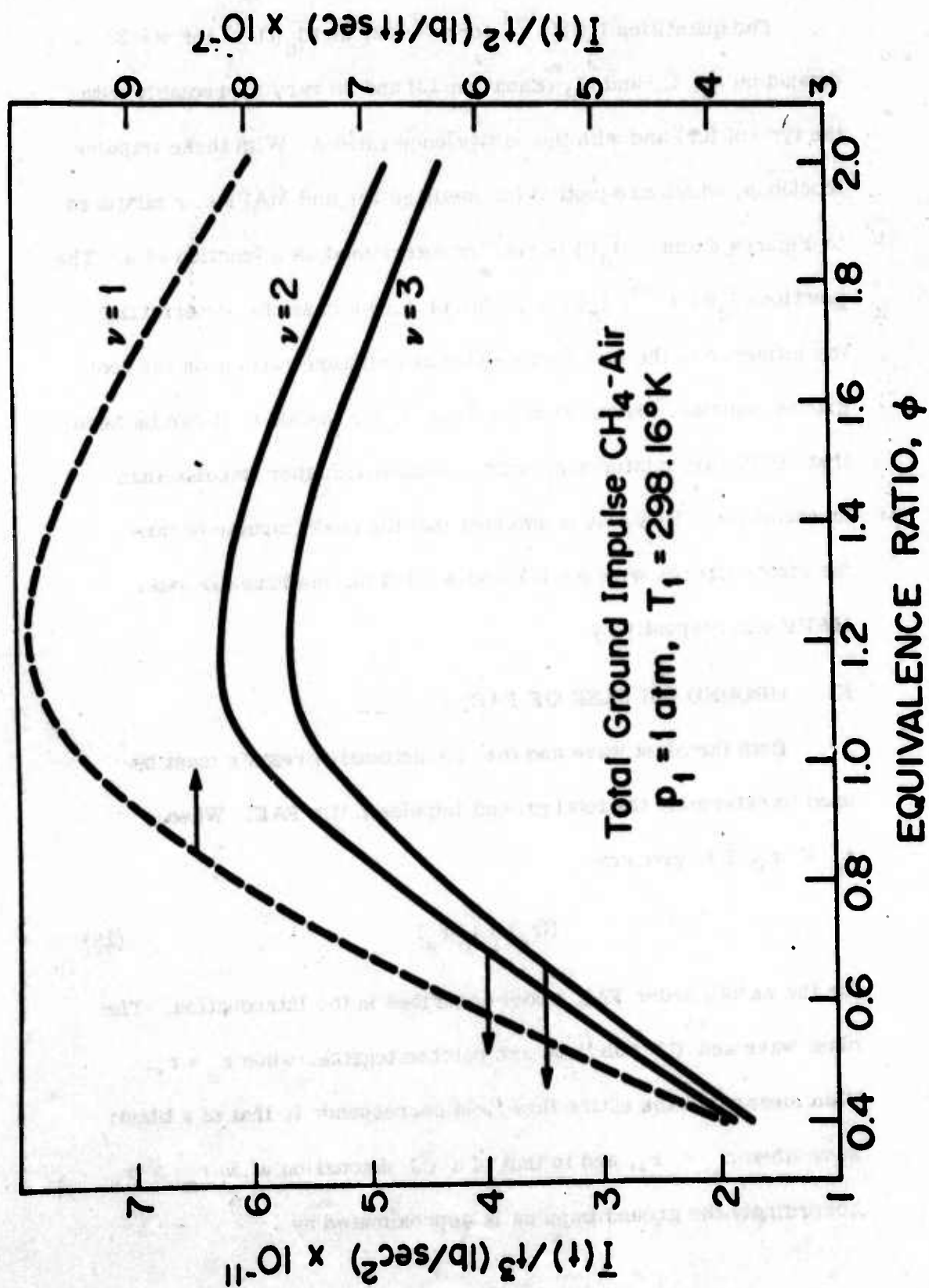
Figure 8. The Variation of Total Ground Impulse for Methane-Air.

24
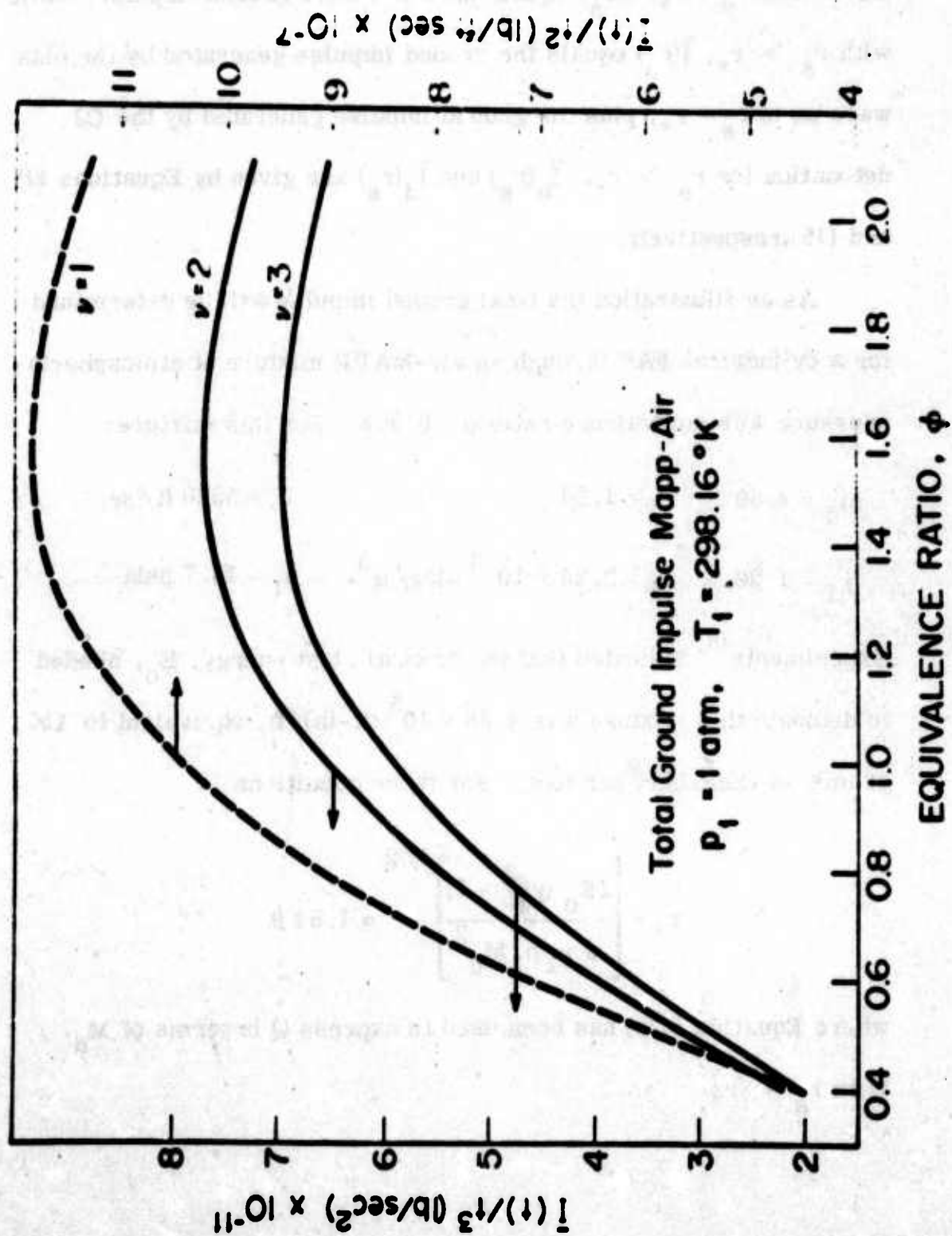
Figure 9. The Variation of Total Ground Impulse for MAPP-Air.

$$\bar{I}(r_s) = \bar{I}_d(r_s) - \bar{I}_d(r_*) + \bar{I}_b(r_*) \tag{20}$$

Thus when $r_s = r_*$, $\bar{I}(r_s)$ equals the blast wave ground impulse, while with $r_s > r_*$, $\bar{I}(r_s)$ equals the ground impulse generated by the blast wave up to $r_s = r_*$, plus the ground impulse generated by the CJ detonation for $r_s > r_*$. $\bar{I}_b(r_s)$ and $\bar{I}_d(r_s)$ are given by Equations (9) and (15), respectively.

As an illustration the total ground impulse will be determined for a cylindrical FAE through an air-MAPP mixture at atmospheric pressure with equivalence ratio $\phi = 0.563$. For this mixture:

$$M_d = 4.69 \qquad \gamma_2 = 1.23 \qquad\qquad C = 5320 \text{ ft/sec}$$

$$\gamma_1 = 1.30 \qquad \rho_1 = 2.29 \times 10^{-3} \text{ slug/ft}^3 \qquad p_1 = 14.7 \text{ psia}$$

Experiments[8] indicated that the critical blast energy, E_o, needed to detonate this mixture was 4.38×10^5 (ft-lb)/ft, equivalent to 150 grams of Detasheet® per foot. For these conditions

$$r_* = \left[\frac{2E_o \, (\gamma_2^2 - 1)}{\pi \, \gamma_1 p_1 M_d^2} \right]^{1/2} = 1.54 \text{ ft}$$

where Equation (12c) has been used to express Q in terms of M_d. With $r_s < r_*$

$$\bar{I}(r_s) = \bar{I}_b(r_s) = 2\pi \left[\frac{E_o \rho_1}{\alpha(\gamma_1, 2)}\right]^{1/2} \beta(\gamma_1, 2) r_s^{\,2} = 9.36 \; r_s^{\,2} \text{(lb-sec)};$$

$$r_s \text{ in ft}$$

or in terms of time

$$\bar{I}(t) = \bar{I}_b(t) = 1.17 \times 10^5 \; t \text{ (lb-sec)}$$

When $r_s > r_*$

$$\bar{I}(r_s) = \bar{I}_d(r_s) - \bar{I}_d(r_*) + \bar{I}_b(r_*) = \frac{2\pi \rho_1 C}{3}\left[\delta(\gamma_2, 2) - \frac{1}{2\gamma_1 M_d^{\,2}}\right](r_s^{\,3} - r_*^{\,3})$$

$$+ 2\pi\left(\frac{E_o \rho_1}{\alpha}\right)^{1/2} \beta(\gamma_1, 2) r_*^{\,2} = (3.06 \; r_s^{\,3} + 11.1)\text{(lb-sec)}$$

as a function of time the impulse becomes

$$\bar{I}(t) = \frac{2\pi \rho_1 C^4}{3}\left[\delta(\gamma_2, 2) - \frac{1}{2\gamma_1 M_d^{\,2}}\right](t^3 - t_*^{\,3}) + 2\pi E_o(\beta/\alpha)t_*$$

$$= (4.60 \times 10^{11} \; t^3 + 19.3) \text{ (lb-sec)}$$

Here t_* corresponds to the time at which the blast wave radius

reaches the critical value r_* so that

$$t_* = r_*^{\,2}\left(\frac{\alpha \rho_1}{E_o}\right)^{1/2} \tag{21}$$

For the example above $t_* = 1.88 \times 10^{-4}$ sec.

The total FAE ground impulse is plotted as a function of both r_s and t in Figures 10 and 11 for the illustrative example computed above. It is of interest to note the small value of r_* in the case treated above, indicating that a fuel-cloud with a radius of the order of 10 feet would, in this case, be dominated by the CJ detonation. This result also suggests that the blast wave phase of the FAE can in some cases be neglected entirely.

F. GROUND IMPULSE AT A FIXED DISTANCE FROM BLAST CENTER

In addition to the total impulse it is of considerable interest to determine the ground impulse per unit area which is generated by a FAE at some fixed distance r from the blast center. If $r > r_*$ the impulse is generated entirely by the passage of a CJ detonation if the zeroth order model of the FAE is used, and the present discussion will be restricted to this case.

The impulse $\bar{\mathcal{I}}$ per unit area at distance r from blast center is given by the integral

$$\bar{\mathcal{I}}(r,t) = \int_{t_s}^{t} \left[p(r,t) - p_1 \right] dt \tag{22}$$

The lower limit, t_s, of this integral is the time at which the wave front first arrives at r and

28
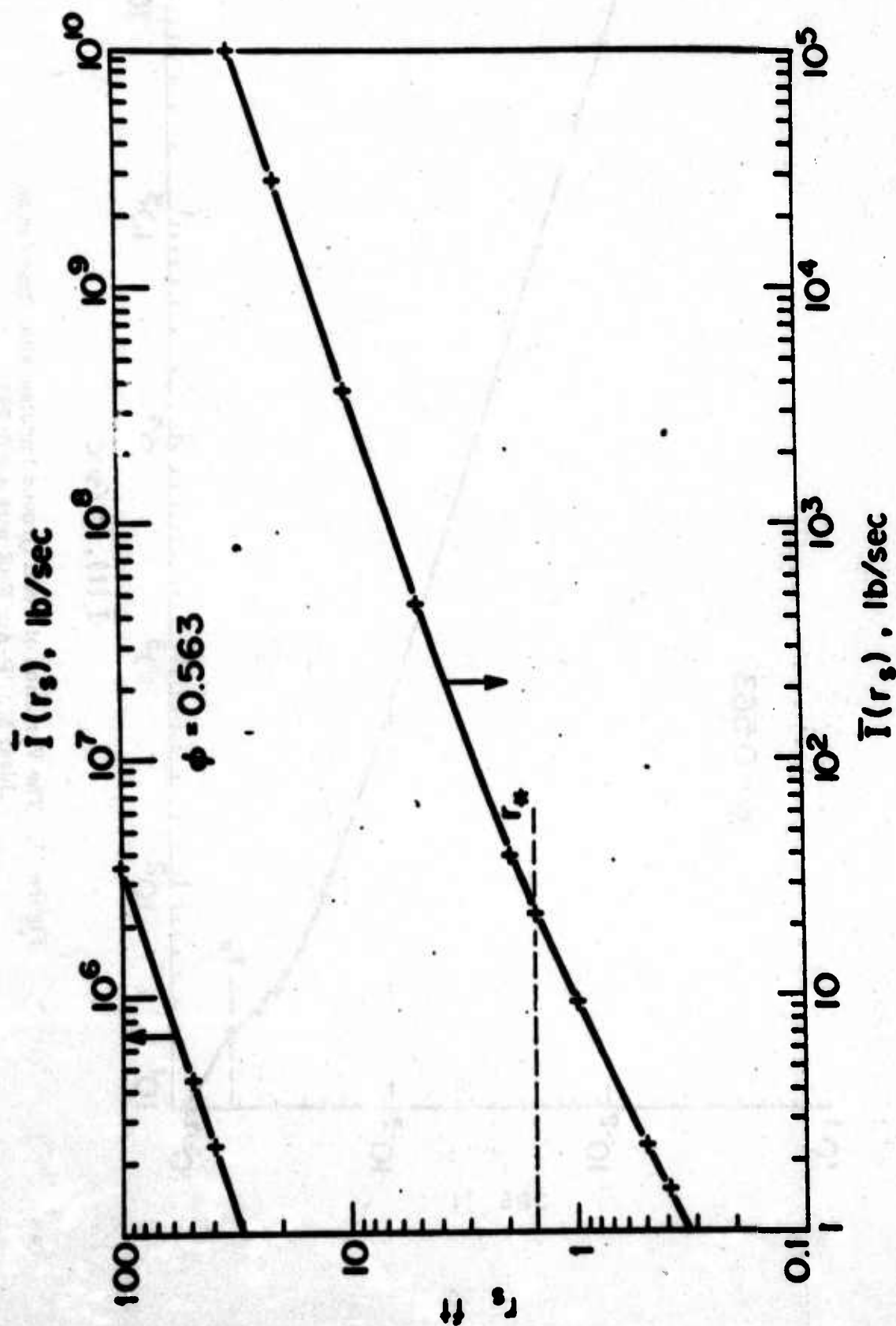
Figure 10. The Variation of Total Ground Impulse with Wave Radius for an Ideal MAPP-Air FAE with $\phi = 0.563$.

29
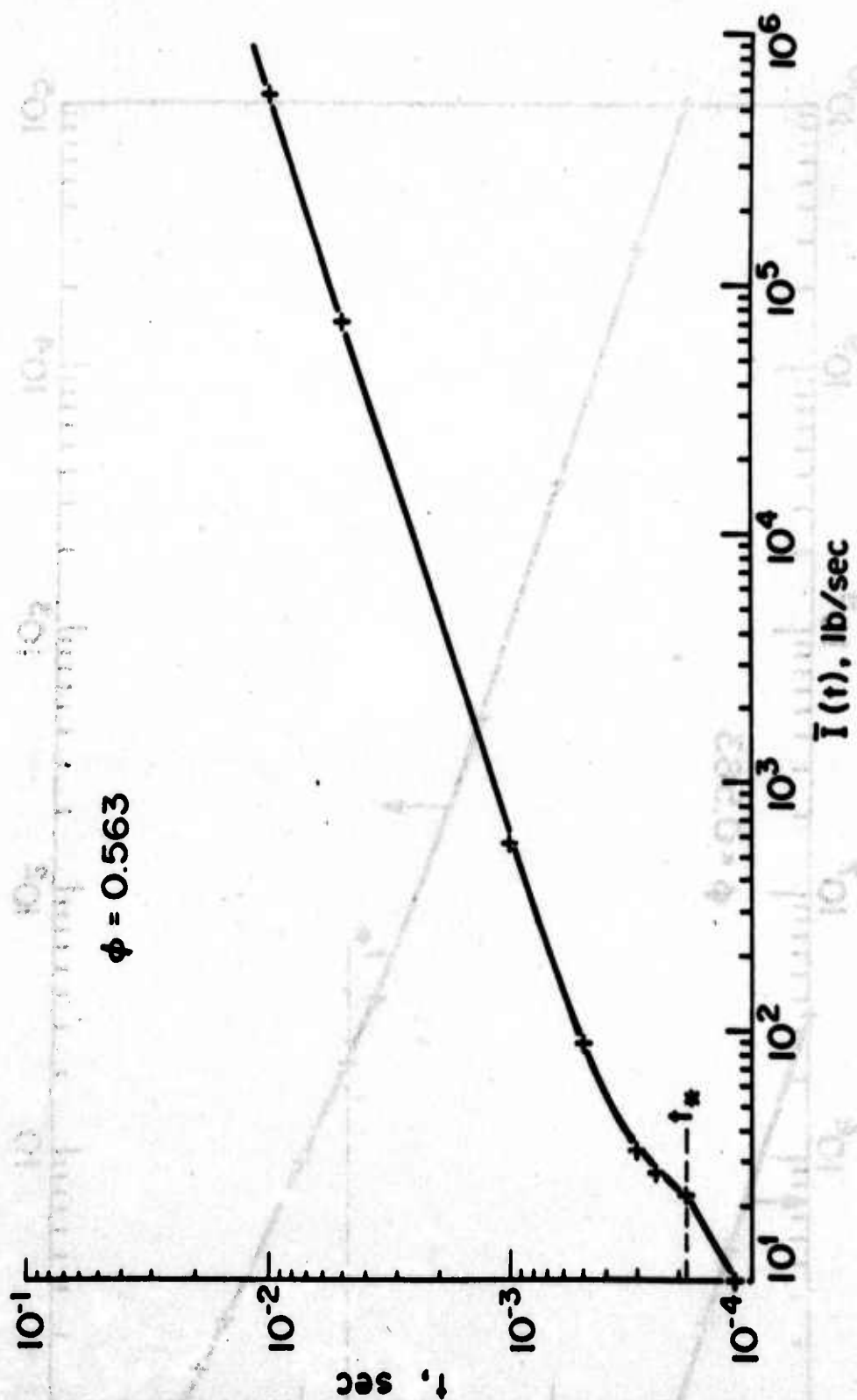
$\phi = 0.563$

Figure 11. The Variation of Total Ground Impulse with Time for an Ideal MAPP-Air FAE with $\phi = 0.563$.

$$t_s = r/C$$

Obviously $\mathcal{Q} = 0$ when $t < t_s$. In Equation (22) and in the analysis below, r plays the role of a parameter and the time t is the only variable. From Equation (10) it follows that (p/p_2) is a function of the similarity variable $\lambda = r/r_s = r/Ct$. Then introducing λ as the variable of integration, Equation (22) can be expressed in the form

$$\mathcal{Q} = \frac{\bar{\mathcal{Q}}}{p_2 t_s} = \int_\lambda^1 \frac{1}{\lambda^2}\left(\frac{p}{p_2}\right) d\lambda - \left(\frac{p_1}{p_2}\right)\left(\frac{1}{\lambda} - 1\right) \qquad (23)$$

The integral in (23) depends on γ_2 and weakly upon the detonation Mach number M_d. Since γ_2 in any case lies in a very narrow range this integral can essentially be treated as a universal impulse function. Thus it is useful to define a function $U(\lambda)$ by

$$U(\lambda) = \frac{\bar{\mathcal{Q}}}{p_2 t_s} + \frac{p_1}{p_2}\left(\frac{1}{\lambda} - 1\right) \qquad (24)$$

The function U can also be considered a function of a dimensionless time $\tau = (t/t_s) = \lambda^{-1}$ so that

$$U(\tau) = \frac{\bar{\mathcal{Q}}}{p_2 t_s} + \frac{p_1}{p_2}(\tau - 1) \qquad (24a)$$

As indicated in Part D above the detonation is followed by an expansion wave in which the fluid velocity drops to zero at some

$\lambda = \lambda_2$. The expansion is followed by a stagnant core from $\lambda = \lambda_2$ to blast center $\lambda = 0$ where the pressure is constant and equal to some value p_3. Surprisingly $(p_3/p_2) \simeq 0.35$ and $\lambda_2 \simeq 0.5$ for $\nu = 1, 2, 3$ and for the range of γ_2 typical of hydrocarbon fuels. Taking this behavior into account it is possible to express $U(\lambda)$ in a somewhat simpler form, especially for $\lambda < \lambda_2$. Thus when $\lambda_2 < \lambda < 1.0$

$$U(\lambda) = \int_\lambda^1 \frac{1}{\lambda^2} \left(\frac{p}{p_2}\right) d\lambda \tag{25}$$

When $0 < \lambda < \lambda_2$

$$U(\lambda) = \int_{\lambda_2}^1 \frac{1}{\lambda^2} \left(\frac{p}{p_2}\right) d\lambda + \frac{p_3}{p_2}\left(\frac{1}{\lambda} - \frac{1}{\lambda_2}\right) \tag{26}$$

or expressed in terms of τ with $\tau_2 = \lambda_2^{-1}$

$$U(\tau) = U(\tau_2) + \frac{p_3}{p_2}(\tau - \tau_2) \tag{27}$$

Since $U(\tau_2) \sim O(1/2)$ it is clear that for large times $\tau \gg \tau_2$, $U(\tau)$ will be dominated by the second term on the right-hand side of Equation (27).

It is useful and revealing to write down the expressions for the impulse in terms of the universal impulse function $U(\tau)$. Thus

$$\bar{\mathcal{I}} = 0 \qquad \tau < 1 \tag{28a}$$

32

$$\mathcal{J} = p_2 \frac{r}{C} \left[U(\tau) - \frac{p_1}{p_2} (\tau - 1) \right] \qquad \tau > 1 \qquad (28b)$$

and when $\tau > \tau_2$, Equation (28b) can also be written in the form

$$\bar{\mathcal{J}} = p_2 \frac{r}{C} \left[U(\tau_2) + \frac{p_3}{p_2} (\tau - \tau_2) - \frac{p_1}{p_2} (\tau - 1) \right] \qquad (29)$$

Generally $U(\tau) \gg (p_1/p_2)(\tau - 1)$ and then it follows from Equation (28b) and Equations (12) that

$$\bar{\mathcal{J}} \propto \frac{M_d \, r \, \rho_1}{(\gamma_2 + 1)} U(\tau) \qquad (30)$$

and Equation (30) shows in a very simple way, how $\bar{\mathcal{J}}$ depends on r, the distance from blast center, and the detonation parameters M_d, ρ_1, and γ_2.

There remains the problem of evaluating the universal function $U(\tau)$. For plane waves with $\nu = 1$, (p/p_2) can be expressed in analytical form[8, 10] and for $\lambda_2 < \lambda < 1$ is given by

$$\frac{p}{p_2} = \left[1 + \frac{C}{a_2} \frac{\gamma_2 - 1}{\gamma_2 + 1} (\lambda - 1) \right]^{2\gamma_2/(\gamma_2 - 1)}$$

$$= \left[1 + \frac{\gamma_2 - 1}{\gamma_2} (\lambda - 1) \right]^{2\gamma_2/(\gamma_2 - 1)} \qquad (31)$$

The second form in Equation (31) follows from using $(\rho_2/\rho_1) \cong (\gamma_2 + 1)/\gamma_2$

33

from Equation (12a). With $\nu = 1$ it follows that $\lambda_2 = (1/2)$ and

$$\frac{p_3}{p_2} = \left[\frac{\gamma_2 + 1}{2\gamma_2}\right]^{2\gamma_2/\gamma_2 - 1} \tag{32}$$

With Equations (31) and (32) $U(\tau)$ is then readily determined. For cylindrical and spherical CJ detonations with $\nu = 2, 3$ it is necessary to use numerically computed values of (p/p_2) as shown in Figure 7. The universal impulse function $U(\tau)$ computed for $\nu = 1, 2, 3$ is shown in Figure 12.

G. DYNAMIC IMPULSE AT A FIXED DISTANCE FROM BLAST CENTER

Any body or obstacle in the path of the FAE will be subjected to a dynamic force due to the leading shock front and the region of high velocity immediately behind the shock. As indicated by Brode, et al[11] the blast load will consist of the forces generated when the shock strikes the obstacle, reflects and eventually flows past the structure. After sufficient time has elapsed, it seems reasonable to assume that the flow will be quasi-steady, i.e., that the flow behaves like a steady flow with a free stream velocity equal to v, the velocity behind the shock or blast wave.

During the quasi-steady portion of the flow the force on the body due to the induced air flow will be

34
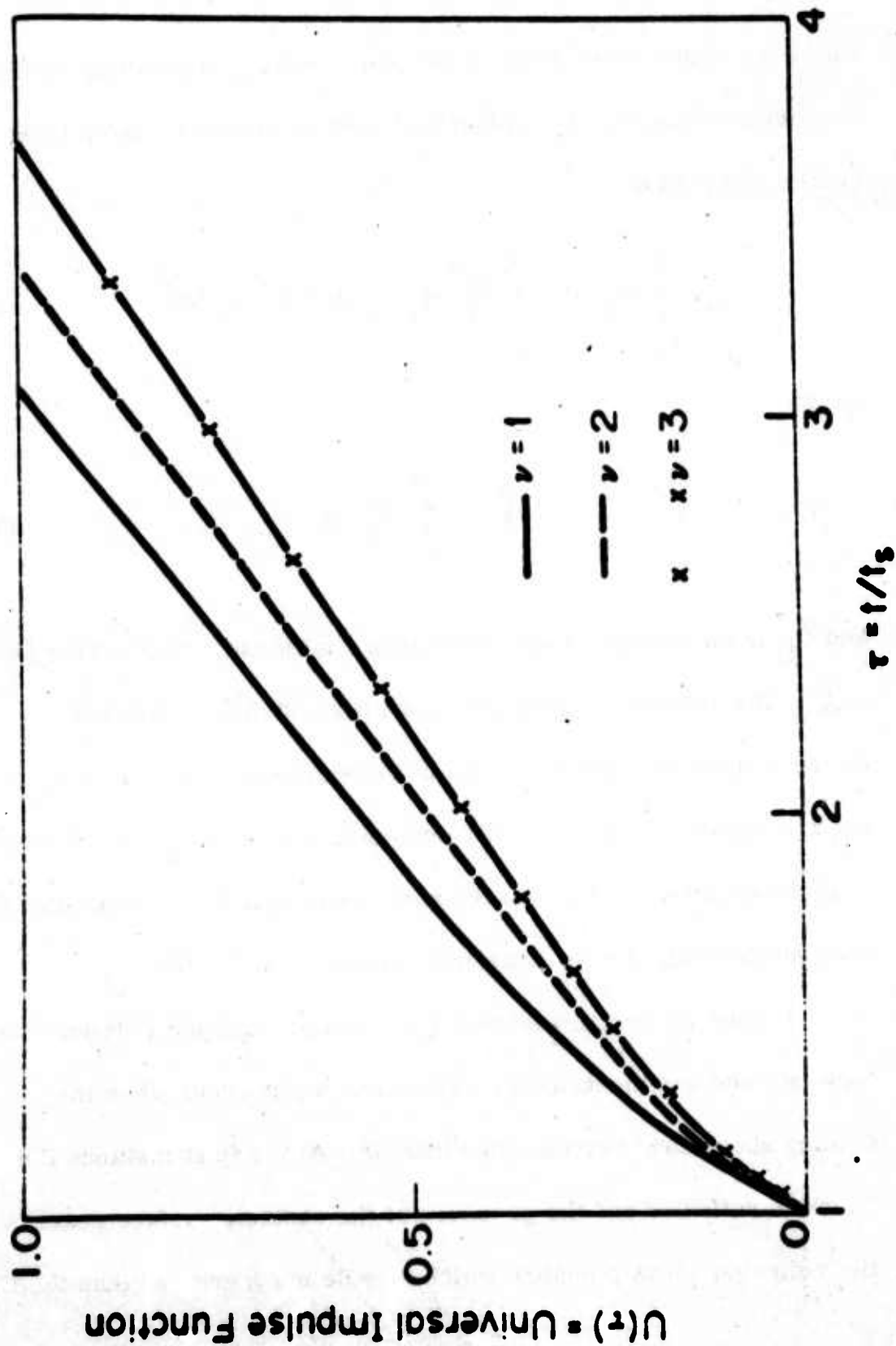
Figure 12. The Universal Impulse Function $U(\tau)$.

$$F_d = \frac{\rho v^2}{2} A_f C_D \tag{33}$$

where A_f is the frontal area of the body, and C_D is the drag coefficient. The dynamic impulse $\bar{I}_v$ applied to a body at distance r from blast center will then be

$$\bar{I}_v = \int_{t_s}^{t} F_d \, dt = \int_{t_s}^{t} \frac{\rho v^2}{2} A_f C_D \, dt = C_D A_f \bar{\mathcal{J}}_v \tag{34}$$

where

$$\bar{\mathcal{J}}_v = \int_{t_s}^{t} \frac{\rho v^2}{2} \, dt \tag{35}$$

and $\overline{C}_D$ is an average value of the drag coefficient. The evaluation of $\bar{\mathcal{J}}_v$, the dynamic impulse per unit area and drag coefficient in terms of universal functions will be considered below. Once A_f and $\overline{C}_D$ are known $\bar{I}_v$ is then readily determined from $\bar{\mathcal{J}}_v$. In the absence of more specific information the assumption that $\overline{C}_D = 1$ can often be used successfully for preliminary results.

It must be emphasized that $\bar{I}_v$, given by Equation (34), does not take into account the unsteady phenomena which occur when the leading shock first reaches the obstacle. At the first instance the shock is reflected and the pressure at the obstacle surface reaches the reflected shock pressure which may be much greater than the CJ

pressure, p_2. If L is the characteristic size of the obstacle then it appears reasonable that a characteristic time τ_t for the initial transient period will be of the order of (L/C). Since the decay of the induced velocity v behind a CJ detonation occurs in the range $(1/2) < \lambda < 1$ the time τ_t during which the dynamic force F_d acts on the obstacle will be of the order r/C. Thus the ratio of $(\tau_t/\tau_d) = (L/r)$ will be small provided $(L/r) \ll 1$, i.e., provided the obstacle size is small compared to the distance from blast center.

Equation (35) for $\overline{\mathcal{J}}_v$ can also be expressed in terms of the similarity variable λ with the result

$$\overline{\mathcal{J}}_v = \frac{\rho_2 v_2^2 t_s}{2} \int_\lambda^1 \left(\frac{\rho}{\rho_2}\right)\left(\frac{v}{v_2}\right)^2 \frac{d\lambda}{\lambda^2} \tag{36}$$

for

$$\lambda_2 < \lambda < 1 \quad \text{or} \quad t_s < t < t_2$$

and $\overline{\mathcal{J}}_v$ remains constant at the value corresponding to λ_2 when $\lambda \leq \lambda_2$. Using the Hugoniot Conditions [Equation (12)] with $\gamma_1 M_d^2 \gg 1$ makes it possible to express Equation (36) in the following more useful form:

$$\frac{\overline{\mathcal{I}}_\nu}{p_2 t_s \dfrac{(\gamma_2 + 1)^2}{2\gamma_2^3}} = U_v(\lambda) = \int_\lambda^1 \frac{1}{\lambda^2} \left(\frac{\rho}{\rho_2}\right)\left(\frac{v}{v_2}\right)^2 d\lambda \qquad (36)$$

and $U_v(\lambda)$ or $U_v(\tau)$ is again a universal impulse function which is essentially independent of detonation properties. The universal impulse function $U_v(\lambda)$ is shown for $\nu = 1, 2, 3$ in Figure 13.

H.   THE INFLUENCE OF SIDE RELIEF

The analysis of impulse described above considers cylindrical or plane waves that are of infinite height or, what is equivalent, that are confined by a non-yielding surface parallel to the ground. Actually such clouds are bounded by inert air or oxidizer. As the detonation propagates through the cloud an expansion wave will thus propagate through the combustion products causing a considerable reduction in the impulse which is generated.

The influence of side relief on a planar detonation has been considered by Sichel[12], Dabora, et al[13], and Sommers and Morrison[14], and this geometry will also be considered here. Analysis of a planar wave with side relief makes it possible to establish the influence of cloud thickness upon impulse. Cylindrical waves with side relief are more complex to analyze; however, for large values of the wave radius the flow near the wave front will

38
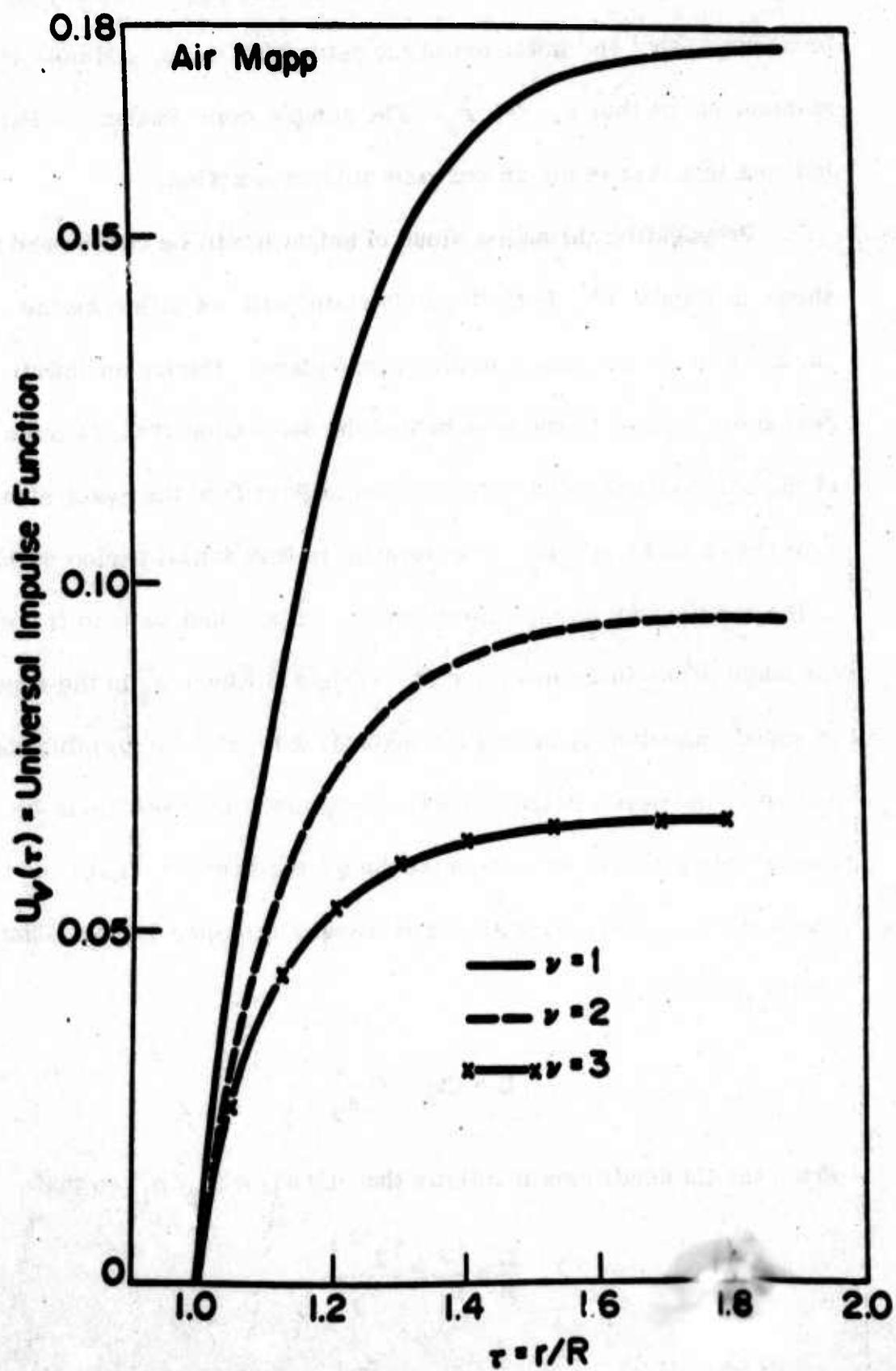
Figure 13.   The Universal Impulse Function $U_v(\tau)$.

approach that behind a plane wave. In the analysis below it will be assumed that the initiation of the detonation wave is almost instantaneous or that $r_* \ll r_s$. The sample computations in Part E indicate that this is not an unreasonable assumption.

Propagation through a cloud of height h will be considered as shown in Figure 14. Initially, side relief will not influence the variation of the pressure on the ground plane. During an initial period of duration t_h the flow behind the detonation changes from that of the self-similar solution described in Part D to the quasi-steady flow shown in Figure 15. The duration of this initial period will be of the same order as the time required for a sound wave to travel the width of the fuel-cloud, i.e., $t_h \sim O(h/a_2)$ where a_2 is the speed of sound immediately behind the detonation front. To simplify the analysis, the self-similar CJ wave pressure distribution will be used to compute the wave impulse during the initial period $t < t_h$. During time t_h, the detonation will travel a distance L from blast center given by

$$L = Ct_h = C \frac{h}{a_2} \tag{38}$$

From the CJ conditions it follows that $(C/a_2) = (\rho_2/\rho_1)$ so that

$$\frac{L}{h} = \frac{\rho_2}{\rho_1} \cong \frac{\gamma_2 + 1}{\gamma_2} \tag{39}$$

40
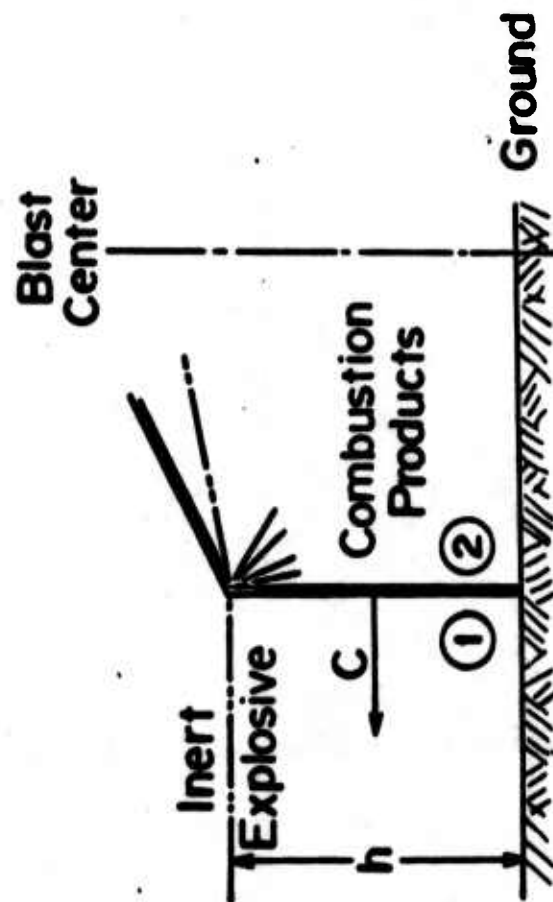
Figure 14. Propagation of a Planar Detonation
Through a Fuel Cloud of Height h.
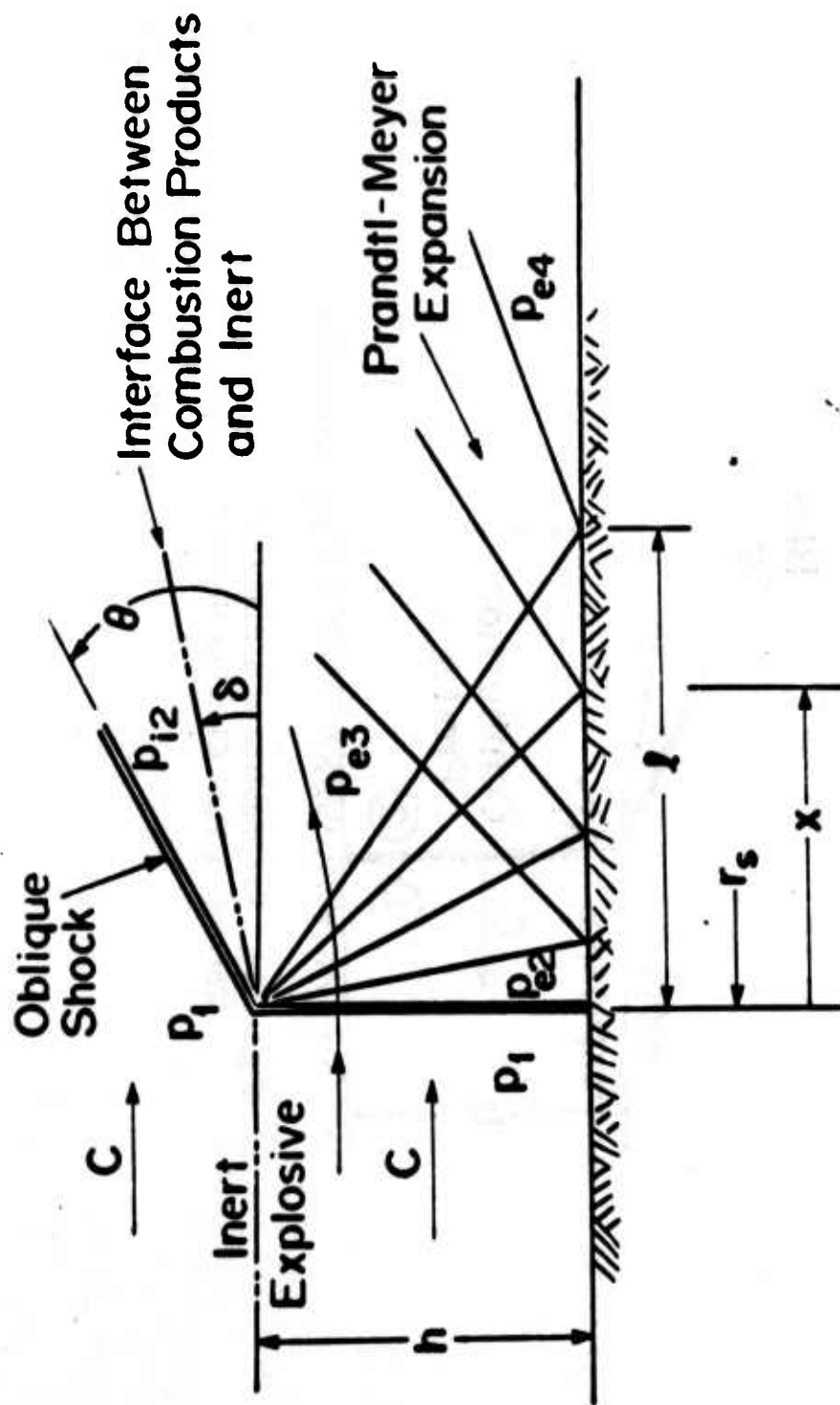
Figure 15. Interaction Between the Products of Detonation and the Inert Boundary—Coordinates Fixed to the Detonation Front.

Since $\gamma_2 = 1.2$ for the products of combustion, it follows that the influence of side relief must be considered after the detonation has travelled a distance equal to about twice the height of the fuel-cloud.

When $t > t_h$ the flow behind the wave will be as pictured in Figure 15, which shows the CJ detonation in a coordinate system fixed to the wave. The CJ detonation is followed by an expansion wave across which the pressure drops from the CJ pressure P_{e_2} to P_{e_3} while the combustion products turn through an angle δ. The molecular weight of the inert $\mathscr{M}_{e1}$ will in the case of air be of the same order as $\mathscr{M}_{e1}$, the molecular weight of the unburned explosive. The CJ detonation generally induces an oblique shock wave in the inert gas[12] across which the flow is deflected through the angle δ. The interface conditions are determined by the requirements that the oblique shock wave and the expansion wave both turn the flow through the same angle δ, and that the pressures P_{i2} and P_{e_3} behind the shock and the expansion be the same. The expansion wave is reflected from the ground plane where the pressure drops from the CJ value P_{e_2} to P_{e_4} at a distance ℓ from the detonation front. The region $r < (r_s - \ell)$ is neglected for the purpose of computing the ground impulse. Here, the pressure will generally be only slightly above atmospheric and will ultimately be

43

relieved by further reflections from the interface between the combustion products and the inert gas. The interaction at the inert-explosive interface causes a reduction in the propagation velocity C which is proportional to the ratio of the reaction zone thickness Δ to the wave height h. This effect will be neglected here.

Since $M_{e2} = 1.0$, the deflection angle δ and the Mach Number M_{e3} downstream of the expansion wave are related by[15]

$$\delta = \left[\frac{\gamma_{e2} + 1}{\gamma_{e2} - 1}\right]^{1/2} \tan^{-1}\left[\frac{\gamma_{e2} - 1}{\gamma_{e2} + 1}\left(M_{e3}^2 - 1\right)\right]^{1/2} - \tan^{-1}\left[M_{e3}^2 - 1\right]^{1/2} \quad (40)$$

From the oblique shock relations

$$\delta = \tan^{-1}\left[2 \cot \theta \frac{M_{i1}^2 \sin^2 \theta - 1}{M_{i1}^2 (\gamma_{i1} + \cos 2\theta) + 2}\right] \quad (41)$$

and by equating Equations (40) and (41) one relation between M_{e3} and θ, the shock angle (Figure 15) is obtained. M_{i1} and γ_{i1} can be determined from the detonation velocity and the properties of the inert gas. The pressure ratio across the oblique shock will be

$$\frac{P_{i2}}{P_1} = 1 + \frac{2\gamma_{i1}}{\gamma_{i1} + 1}\left(M_{i1}^2 \sin^2 \theta - 1\right) \quad (42)$$

The flow across the expansion wave is isentropic. Then using Equation (12b) for the pressure ratio across the detonation it is readily shown that

44

$$\frac{P_{e3}}{P_1} = \frac{P_{e2}}{P_1}\frac{P_{e3}}{P_{e2}}$$

$$= \left(\frac{1 + \gamma_{e1} M_{e1}^2}{\gamma_{e2} + 1}\right)\left[\frac{(\gamma_{e2} + 1)/2}{1 + (1/2)(\gamma_{e2} - 1) M_{e3}^2}\right]^{\frac{\gamma_{e2}}{\gamma_{e2} - 1}} \tag{43}$$

Since $(P_{12}/P_1 = (P_{e3}/P_1)$, Equations (42) and (43) provide the additional equation required to determine M_{e3} and θ. Once M_{e3} is determined, δ, P_{e3} and the details of the expansion wave are readily established. The pressure variation along the ground plane due to the reflected expansion wave can be determined using the method of characteristics as described, for instance, in Reference 15.

Following the discussion above the impulse $\bar{I}(r_s)$ will be given by

$$\bar{I}(r_s) = \bar{I}_d(r_s) \quad ; \quad r_s < L = Ct_h \tag{44}$$

with $\bar{I}_d(r_s)$ from Equation (15). There will be cases in which the reflection length $\ell > L$. In this case confined wave impulse $\bar{I}_d(r_s)$ will be used until the wave has moved distance ℓ from blast center, i.e., until the expansion wave reflection pattern is completely established. With $r_s > L$ or ℓ the total ground impulse, I_s, of a planar detonation with side relief will be

45

$$\overline{I}_s = \left[\int_{r_{s-\ell}}^{r_s} (P - P_1) \, dr \right] (t - t_h) + I_d(t_h) \tag{45}$$

The integral in Equation (45) is more conveniently expressed in terms of the variable

$$\xi = \frac{x}{h} = \frac{r_s - r}{h}$$

where x is the distance of a given point from the wave front as shown in Figure 15. Then Equation (45) can be written in the form

$$\overline{I}_s = P_{e2} \, h \left(\frac{r_s}{c} - \frac{\gamma_2 + 1}{\gamma_2} \frac{h}{c} \right) \int_0^{\frac{\ell}{h}} \left[\frac{P}{P_{e2}} (\xi) - \frac{P_1}{P_{e2}} \right] d\xi + I_d \left(\frac{\gamma_2 + 1}{\gamma_2} h \right) \tag{46}$$

Since h is the only characteristic length to enter the interactions between the combustion products and the inert boundary, h can be used to scale the dimensions of the interaction region. It follows that the wall pressure variations P/P_{e2} will depend only on the dimensionless variable x/h for a given fuel-oxidizer mixture. A consideration of the expansion wave behind the detonation shows that

$$\frac{\ell}{h} \simeq O \left[\tan \left(\delta + \frac{\pi}{2} - \sin^{-1} \frac{1}{M_{e3}} \right) \right] \tag{47}$$

Hence, the integral in Equation (46) which will be denoted by $U_s(\Phi)$ so that

46

$$U_s(\Phi) = \int_0^{\frac{\ell}{h}} \left[\frac{P}{P_{e2}} (\xi) - \frac{P_1}{P_{e2}} \right] d\xi$$

will depend only on the equivalence ratio Φ for a given fuel.

It is, perhaps, most convenient to write the expression for $\bar{I}_s$ in the form

$$I_s = P_1 h \frac{P_{e2}}{P_1} \left(\frac{r_s}{c} - \frac{\gamma_{e2}+1}{\gamma_{e2}} \frac{h}{c} \right) U_s(\Phi) + I_d \left(\frac{\gamma_{e2}+1}{\gamma_{e2}} h \right)$$

$$r_s > \frac{\gamma_{e2}+1}{\gamma_{e2}} h \qquad (46a)$$

The fuel properties will determine P_{e2}/P_1, C, and $U_s(\Phi)$. The height h enters the expression for $\bar{I}_s$ in two ways. First h appears explicitly in the coefficient of $U_s(\Phi)$, then h determines the distance L the detonation travels before side relief becomes important. If R is the outer radius of the fuel-cloud and if $h > \gamma_{e2} R / (\gamma_{e2} + 1)$, the foregoing considerations indicate that side relief will not affect the total ground impulse.

The function $U_s(\Phi)$ has been computed for MAPP-air, and methane-air mixtures. Over the range $0.6 \leq \Phi \leq 1.6$ the Prandtl Meyer angle δ and the shock angle θ were found to remain essentially constant at $\delta = 20^O$, $\theta = 29^O$ for both mixtures. As a

47

consequence the ratio $\ell/h = 2.90$ and is also constant so that the integral

$$\int_0^{\frac{\ell}{h}} \frac{p}{p_{e2}}(\xi)\,d\xi = 1.3885$$

and is also constant for the above two fuels. The impulse function $U_s(\Phi)$ then has the remarkably simple form

$$U_s(\Phi) = 1.3885 - \int_0^{\frac{\ell}{h}} \frac{p_1}{p_{e2}}\,d\xi$$

$$= 1.3885 - \frac{\ell}{h}\frac{p_1}{p_{e2}} = 1.3885 - 2.90\frac{p_1}{p_{e2}} \qquad (48)$$

It must be emphasized that this result is valid only for CH_4-air and MAPP-air mixtures in the range $0.6 \leq \Phi \leq 1.6$. However, it is likely that Equation (48) will remain valid for other hydrocarbon-air mixtures over this range of equivalence ratio.

For large values of r_s/h the total impulse $\bar{I}_s$ generated by a planar wave with side relief is approximately

$$\bar{I}_s = \frac{P_1 h r_s}{C}\left(\frac{P_{e2}}{P_1}\right) U_s(\Phi) \qquad (49)$$

while the total impulse of a planar confined CJ detonation will,

48

from Equation (15) be approximately

$$\bar{I}_d = \frac{P_1 r_s^2}{C} (\gamma_{e2} + 1) \left(\frac{P_{e2}}{P_1}\right) \left[\delta (\gamma_{e2}, 1) - \frac{1}{\gamma_{e1} M_{e1}^2}\right] \qquad (50)$$

Thus, $\bar{I}_s \propto h r_s$ and $\bar{I}_d \propto r_s^2$ so that $\bar{I}_d$ increases more rapidly with r_s than $\bar{I}_s$. This result is to be expected since a core of high pressure stagnant gas is maintained behind the confined detonation front; whereas this high pressure region is destroyed when there is side relief. Thus when $r_s/h \gg 1$

$$\bar{I}_s / \bar{I}_d \propto \frac{h}{r_s} \qquad (51)$$

When $(\ell / r_s) \ll 1$, the flow behind a cylindrical detonation with side relief will approach that behind a planar wave. Then it is readily shown that

$$\bar{I}_s \cong P_1 h \left(\frac{P_{e2}}{P_1}\right) \pi \frac{\left(r_s^2 - L^2\right)}{C} U_s(\Phi) + \bar{I}_d(L) \qquad (52)$$

For $r_s \gg h$ it follows from Equation (52) that

$$\bar{I}_s = \frac{P_1 h \pi r_s^2}{C} \left(\frac{P_{e2}}{P_1}\right) U_s(\Phi) \qquad (53)$$

while for a cylindrical confined detonation

49

$$\overline{I}_d = \frac{2\pi P_1 r_s^2}{3C} (\gamma_{e2} + 1) \left(\frac{P_{e2}}{P_1}\right) \left[\delta(\gamma_{e2}, 2) - \frac{1}{2\gamma_{e1} M_d^2}\right] \qquad (54)$$

Thus, Equation (51) for $\overline{I}_s / \overline{I}_d$ remains valid in the cylindrical case.

I.   DISCUSSION

Simple relations have been developed above for the computation of the impulse generated by an idealized FAE. The key idea is to represent the FAE by the strong blast self-similar solution for $r_s < r_*$ and by the C-J wave self-similar solution for $r_s > r_*$. In addition, the fuel is assumed to be uniformly distributed in clouds with planar cylindrical or spherical symmetry. At first only clouds with infinite confinement are considered. The self-similar form of the solutions then leads to remarkably simple expressions for the total ground impulse and the static and dynamic impulse at some fixed distance from blast center.

As indicated by Brode, et al[11] the self-similar blast wave solution used here provides only a crude approximation to the flow, and with recent advances in numerical computations, more accurate theoretical solutions have become available. However, as was shown by the illustrative example, r_* will generally be small compared to the fuel-cloud radius so that the initiating blast will not have a large

50

effect on the total impulse which is generated. The propagation velocities computed using the zeroth order FAE model agreed remarkably well with experiments designed to simulate a cylindrical FAE with infinite confinement[1].

The influence of side relief was investigated for planar waves but, as indicated in Part H, the results can be extended to cylindrical FAE's for sufficiently large values of the wave radius r_s. The interaction between the products of combustion and the inert boundary also has a self-similar character so that the influence of side relief and cloud height can also be represented in a remarkably simple form.

The results presented here make it possible to determine the effects of fuel properties, cloud geometry, and side relief upon impulse with a minimum of computational effort.

SECTION III

EXPERIMENTAL RESEARCH

A. INTRODUCTION

The research described herein is part of an ongoing study[8,9] of cylindrical shock and homogeneous and heterogeneous detonation waves, primarily aimed at gaining a better understanding of the fundamental aspects involved in the unconfined explosion of fuel-oxidizer mixtures. Some of the early results of these studies have been presented at meetings[1,16]; this work represents extensions made since the previous annual report. Experimental research into the FAE problem has been subdivided into two major phases; studies relating to the initiation of self sustaining homogeneous and heterogeneous detonations; and studies relating to the breakup and ignition of liquid fuel drops. The former phase has naturally received most of the emphasis. The latter phase was undertaken to examine the effects upon drop time history of the trailing rarefaction associated with the blast wave and the attendent reduction in gas pressure and temperature. This information in turn will assist in a more complete analytical description of the FAE.

Regarding the first phase, experience and experimental evidence substantiates the existence of four regimes of explosion which may occur upon ignition of an unconfined fuel-air cloud, dependent upon the intensity

of the initiating source. For a low energy ignition source, such as a hot surface or small open flame, the cloud will likely be consumed by a normal deflagration process (although, on occasion, they have been observed to accelerate, presumably due to turbulent mixing and buoyancy effects, to full fledged detonations). For a somewhat higher and rapid energy release (but yet sub-critical), a blast wave followed by combustion may be generated which then rapidly decays to a normal deflagration process. For higher rapid energy releases (just-critical), the blast wave may decay followed by a transition stage, at some distance from the ignition source, which subsequently leads to an asymptotic strengthening to a CJ detonation. For yet higher rapid energy releases (super-critical), the blast wave decays until the energy contained therein is of the same order of magnitude as that due to combustion, at which point the wave begins its asymptotic weakening to a CJ detonation. The interest of the work to be described is restricted to the latter three cases or to the case of a blast wave impacting a single stream of fuel drops in an oxidizing atmosphere.

The experimental facility described in previous reports[8, 9] was used with no major alterations during the time frame reported upon herein. Following the acquisition of data from a series of blast wave shadowgraph photographs, a slightly improved breech was developed, and more efficient electric ignitors used. An extension to the current chamber was designed,

53

which will increase the chamber length to nearly 6 feet, in order to accommodate greater run times. The general facility capabilities allow initial drop diameters of 200 μm $\leq D_o \leq$ 1800 μm, with any non-corrosive oxidizing atmosphere of $0 \leq P \leq 2$ atm and with incident blast wave Mach numbers much greater than common Mach numbers of detonation. The implementation of the optical system used with the chamber is discussed in detail in Part C, where it received the greatest use. A final word is in order concerning experimental strong blast wave data, which consumed much time to compile and analyze in the early stages of this work. Typical radius-time data obtained in the sectored chamber can be non-dimensionalized and displayed as shown in Fig. 16. This figure demonstrates the ability of the chamber facility to effectively generate blast waves of a highly cylindrical character; something which has been stated nearly from the start. Figure 16 also demonstrates that the cylindrical wave character is modeled more accurately as the blast source energy is increased.

B. BLAST WAVE INITIATION AND PROPAGATION OF CYLINDRICAL DETONATIONS

Earlier publications[1, 4, 9, 16] have discussed attempts to formulate satisfactory models for the blast initiation of detonations in clouds of fuel in gaseous or droplet form, and pointed out their inherent difficulties. Also suggested therein was a simplified model based upon a composite of similarity solutions for the strong blast and CJ detonation
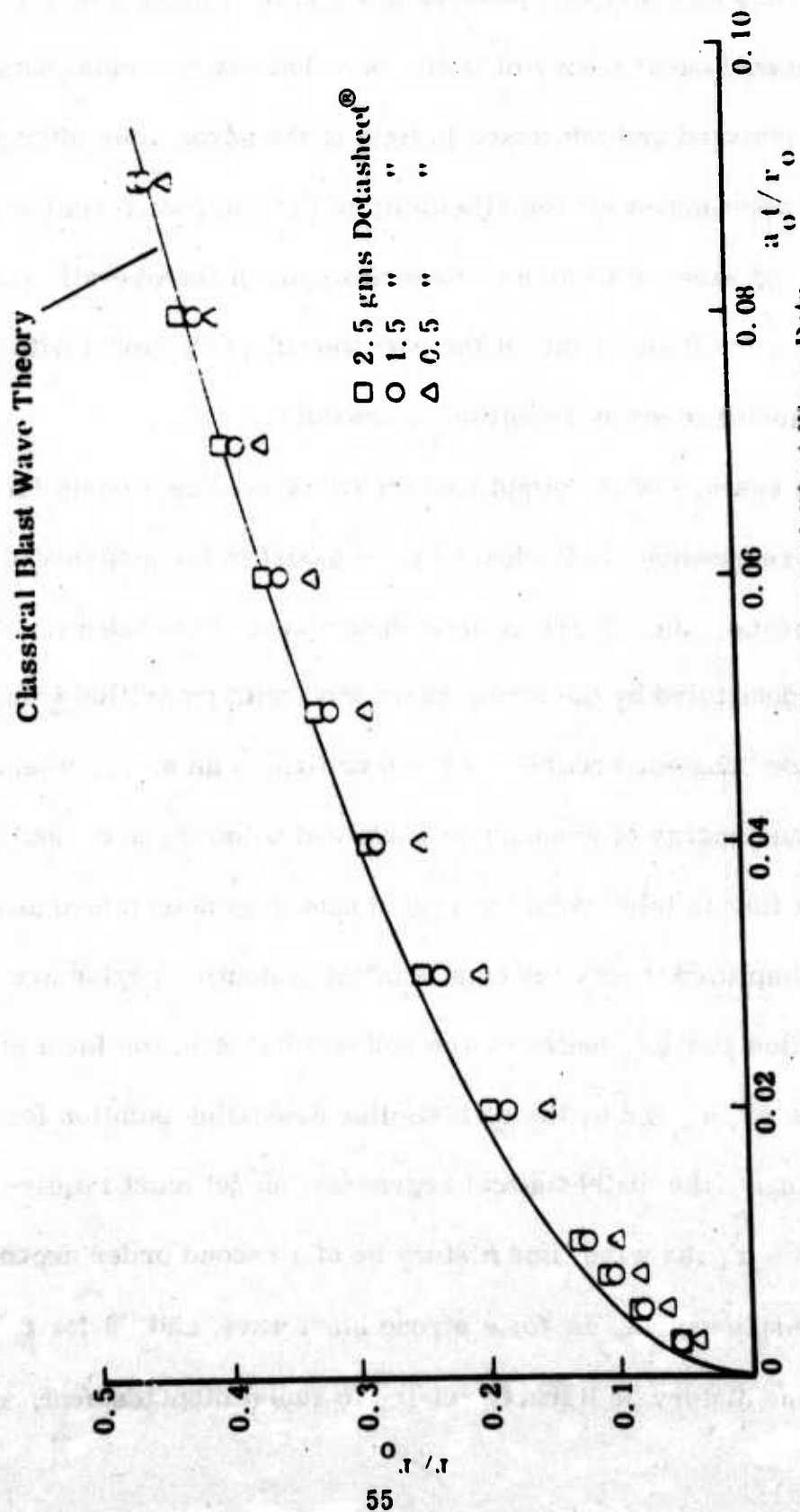
Figure 16. Nondimensionalized Experimental Blast Wave Data.

waves. Bach, et al[17], in an attempt to overcome some of the difficulties

alluded to above and still possess a model of sufficient detail, introduced

a phenomenological theory of initiation. The experimental data presented

here is analyzed and discussed in light of the advantages offered by both

of these approaches: (1) the simplicity of the composite similarity solution

model, and ease with which an understanding of the overall process is

attained, and (2) the detail of the phenomenological model with which an

understanding of wave transition is possible.

The essence of the simplified theory is used as a basis for a mathe-

matical regression model developed to assist in the analysis of the

experimental data. First, a brief description of the theory. The flow is

at first dominated by the strong blast wave with transition from blast to

detonation behavior occurring near a critical radius, r_*, where the blast

energy and energy of combustion contained within r_* are equal. The

complex flow in this transition region cannot be determined analytically.

In the simplified theory the details of the transition region are ignored

but the flow is represented by the self-similar solution for a strong blast

wave for $r < r_*$ and by the self-similar detonation solution for $r > r_*$.

Accordingly, the mathematical regression model must require that:

(1) for $r < r_*$ the wave time history be of a second order dependency on

radial displacement, as for a strong blast wave, and (2) for $r > r_*$ the

wave time history be linearly related to radial displacement, as for a

56

CJ detonation. Specifically, the model makes use of the method of LaGrange multipliers to minimize the standard error of a least squares curve fit of rough experimental time-radius data to the following:

$$t_i = \alpha_0 + \alpha_1 r_i + \alpha_2 r_i^2 + \epsilon_i \quad \text{for} \quad r_i < r_*$$

and

$$t_i = \beta_0 + \beta_1 r_i + \epsilon_i \quad \text{for} \quad r_i > r_* \tag{55}$$

The problem is then to compute the constant coefficients α_0, α_1, α_2, β_0, β_1 and the critical radius r_*, in order to minimize the standard error subject to the constraints that at $r_i = r_*$

$$\alpha_0 + \alpha_1 r_* + \alpha_2 r_*^2 = \beta_0 + \beta_1 r_*$$

and

$$\alpha_1 + 2\alpha_2 r_* = \beta_1 \tag{56}$$

Confidence limits (standard errors) were successfully established on the evaluated critical radius and slope of the linear portion of the model (i. e., detonation velocity). Typically, detonation velocity is evaluated to within 2 percent error, but the error on critical radius often exceeds 10 percent. Consequently, in practice, the detonation velocity derived from the model is used unquestioned but the critical radius value is tempered by manually tabulated values whose error is of the order of the model's value.

57

Application of this model to representative experimental data will be discussed below. Before doing this, the connection between the simplified theory, Bach, et al's phenomenological theory, and the experimental data must first be made clear. The solid lines (1-8) of Figure 17 represent the essence of the latter theory's behavior on an M_s versus r_s/r_o plot where r_s is the radius of the wave and r_o is the explosion length. The curves essentially represent increasing blast source energy. The model recovers the two limiting cases of a supercritical energy regime (i.e., a monotonic decay to a CJ wave, curve 1) for very large source energy and the subcritical energy regime (i.e., the blast asymptotically weakens to an acoustic wave, curves 5-8) for very low source energy. In between these two limits (critical energy regime) the blast initially decays to a sub-CJ velocity and then asymptotically accelerates to its eventual CJ condition (curves 2-4). The model predicts that the minimum velocities attained in the critical regime depend on the magnitude of the source energy. This solution suggests that unless the initiation energy is extremely large, a decay below the CJ condition always occurs and the eventual approach is rather slow. By comparison, the simplified theory (curve a) predicts an immediate initiation of the CJ condition upon reaching the point r_*/r_o, where

58
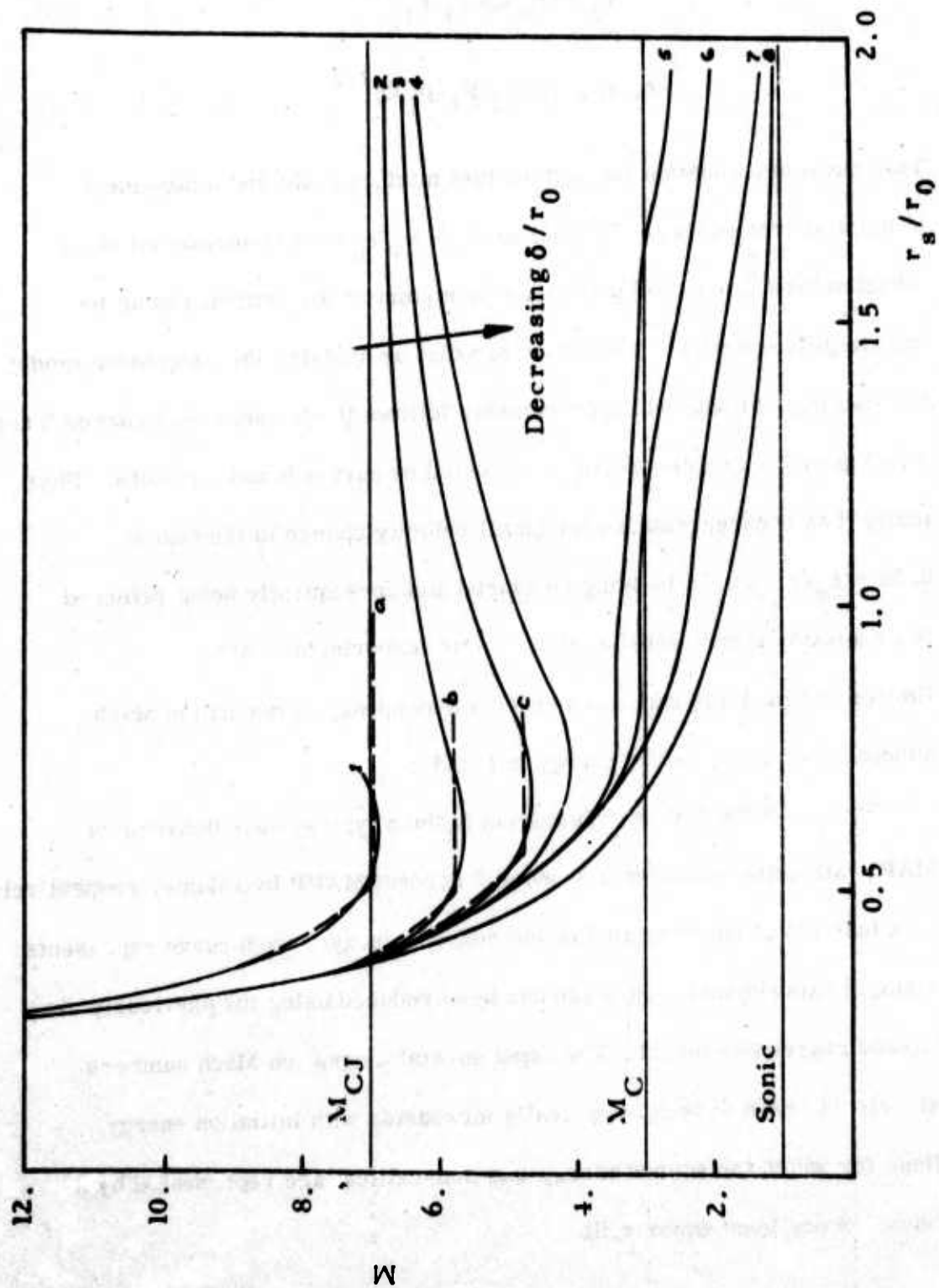
Figure 17. Comparison of Blast Initiation Theories, Simplified and Phenomenological

$$r_* = (E_o/\pi \, \rho_1 \, Q)^{1/2}$$

$$r_o = (E_o/2\pi \, \gamma_1 \, P_1)^{1/2} \tag{57}$$

$$r_*/r_o = (2\pi \, \gamma_1 \, P_1/\rho_1 \, Q)^{1/2}$$

This ratio is a constant for a given fuel mixture ratio and independent of blast source energy. Thus on an $M_s - r_s/r_o$ representation all blast initiated detonations collapse to a single point at the critical radius for the simplified theory. It is now clear that by applying the regression model to experimental data which presumably follows the trends of say curves 2 and 3 in Figure 17, the interpretation suggested by curves b and c results. Physically it is apparent that a very small velocity change in the region $0.50 \leq r_s/r_o \leq 0.75$ is being measured and consequently being referred to as a quasi-steady sub-CJ state. Our experiments are limited to this same range and hence a dependency of detonation Mach number upon blast source energy is found.

Figure 18 displays in transparent fashion typical wave behavior of MAPP-air detonations for 9.7 and 4.3 percent MAPP by volume, respectively, as a function of chamber radius and source energy. Each curve represents a single experimental run which has been reduced using the previously discussed regression model. The experimental detonation Mach numbers are clearly seen to be monotonically increasing with initiation energy. Runs for which the source energy was sub-critical are represented by a second order least squares fit.

60
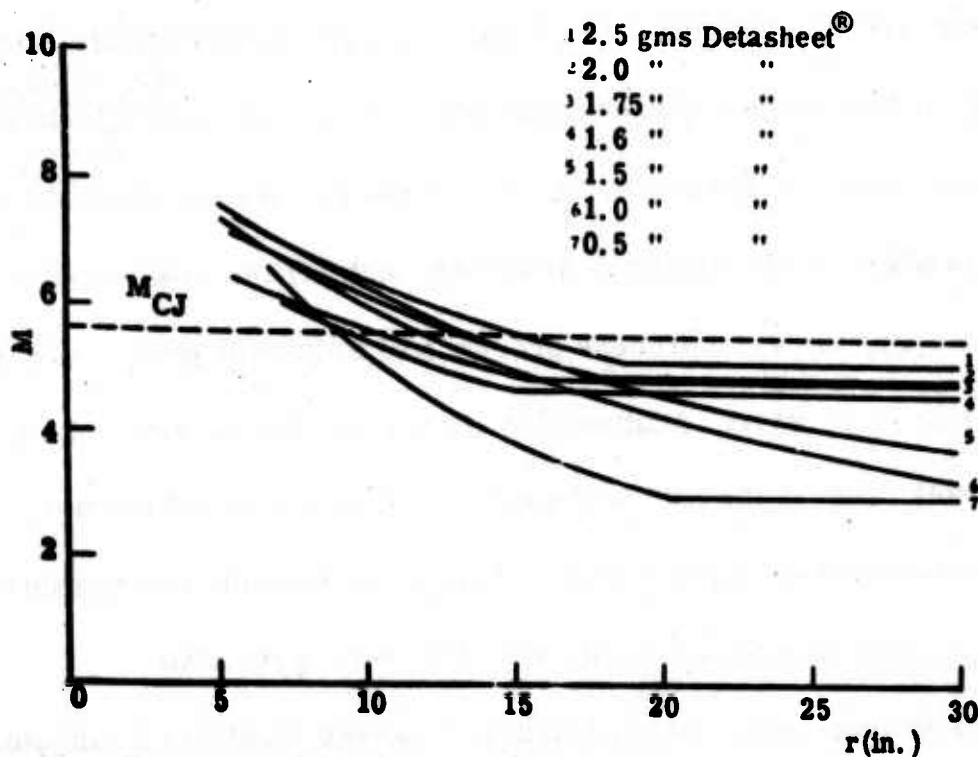
Figure 18a. Experimental Mach No. —Radius Behavior, 9.7 Percent MAPP-Air.
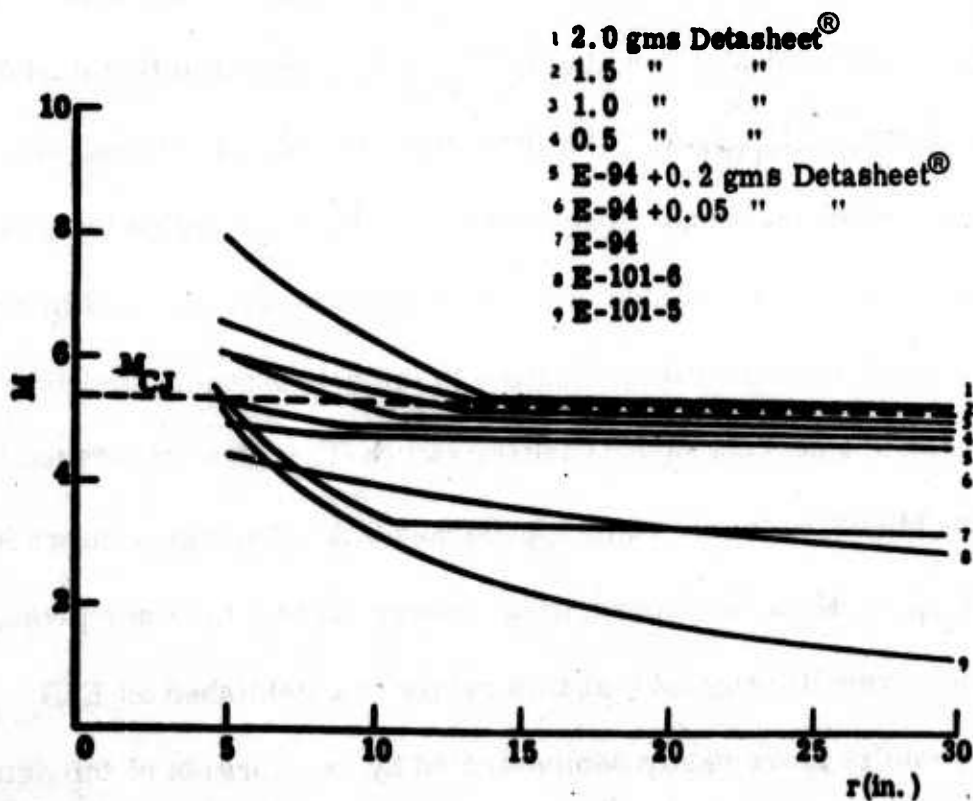
Figure 18b. Experimental Mach No. —Radius Behavior, 4.3 Percent MAPP-Air.

61

General features displayed by Figure 18 are: (1) identifiable threshold energies, below which a quasi-steady CJ state is not established; (2) detonation transition distances are readily shown, beyond which the calculated detonation Mach number is achieved; and (3) for low enough source energy, the wave process proceeds to follow the pattern of a decaying reacting blast wave. Additionally, it is seen that curves 7 of Figure 18a and 18b both suggest the establishment of detonation wave behavior, yet at a clearly sub-threshold energy level. This is presumably substantiated by the similar occurrence of a stable sub-CJ wave predicted by the phenomenological theory (Figure 17, curves 5 and 6). A fundamental difference between Figures 18a and 18b is suggested by the fact that in the former, experimental Mach numbers, M_{exp}, are less than that of the corresponding CJ state, (M_{CJ}), while in the latter, the M_{CJ} is straddled by the experimental Mach numbers. The reason for this is revealed by an examination of the orders of magnitude of blast source energy, E, used in experiments at a given mixture ratio, relative to the corresponding critical energy, E_{crit}. In the 9.7 percent MAPP case the ratio E/E_{crit} never exceeded 1.2, while in the 4.3 percent MAPP case this ratio approached 9.5. The situation whereby $M_{exp} \geq M_{CJ}$, typifies the supercritical energy regime for wave propagation and the above results suggest that this region is established as $E/E_{crit} \sim 10.0$. This statement is more easily demonstrated by examination of the actual experimental data given in Table II and displayed graphically in Figure 19.

TABLE II. DETONATION MACH NUMBER AND ENERGY DATA FOR MAPP-AIR EXPERIMENTS.

Percent Fuel Concentration by Volume	E_{crit} $\times 10^{-5}$ (ft-lbf/ft)	E at M_{max} $\times 10^{-5}$ (ft-lbf/ft)	M_{max}	E at M_{CJ} $\times 10^{-5}$ (ft-lbf/ft)	M_{CJ}	$\dfrac{E_{M_{max}}}{E_{M_{CJ}}}$	$\dfrac{E_{M_{CJ}}}{E_{crit}}$	$\dfrac{E_{M_{max}}}{E_{crit}}$	Supercritical Condition Established
9.7	4.55	5.59	5.18	8.9*	5.58	0.629*	1.957*	1.200	No
8.5	2.58	5.5	5.54	5.6*	5.62	0.980*	2.169*	2.132	No
6.8	1.13	4.86	5.32	4.35*	5.62	1.117*	3.846*	3.436	Yes
6.0	0.8	4.5	~5.88	3.5	5.57	1.285	4.386	5.618	Yes
4.3	0.5	4.62	5.40	3.4	5.26	1.359	6.803	9.259	Yes
3.8	1.4	4.4	~5.1	2.1	5.1	2.092	1.499	3.663	Yes
3.3	2.2	6.2	~5.2	1.7	4.74	3.649	0.775	2.816	No
2.9	4.4	6.19	5.45	3.3	4.72	1.876	0.752	1.406	No

*Extrapolation of existing data.
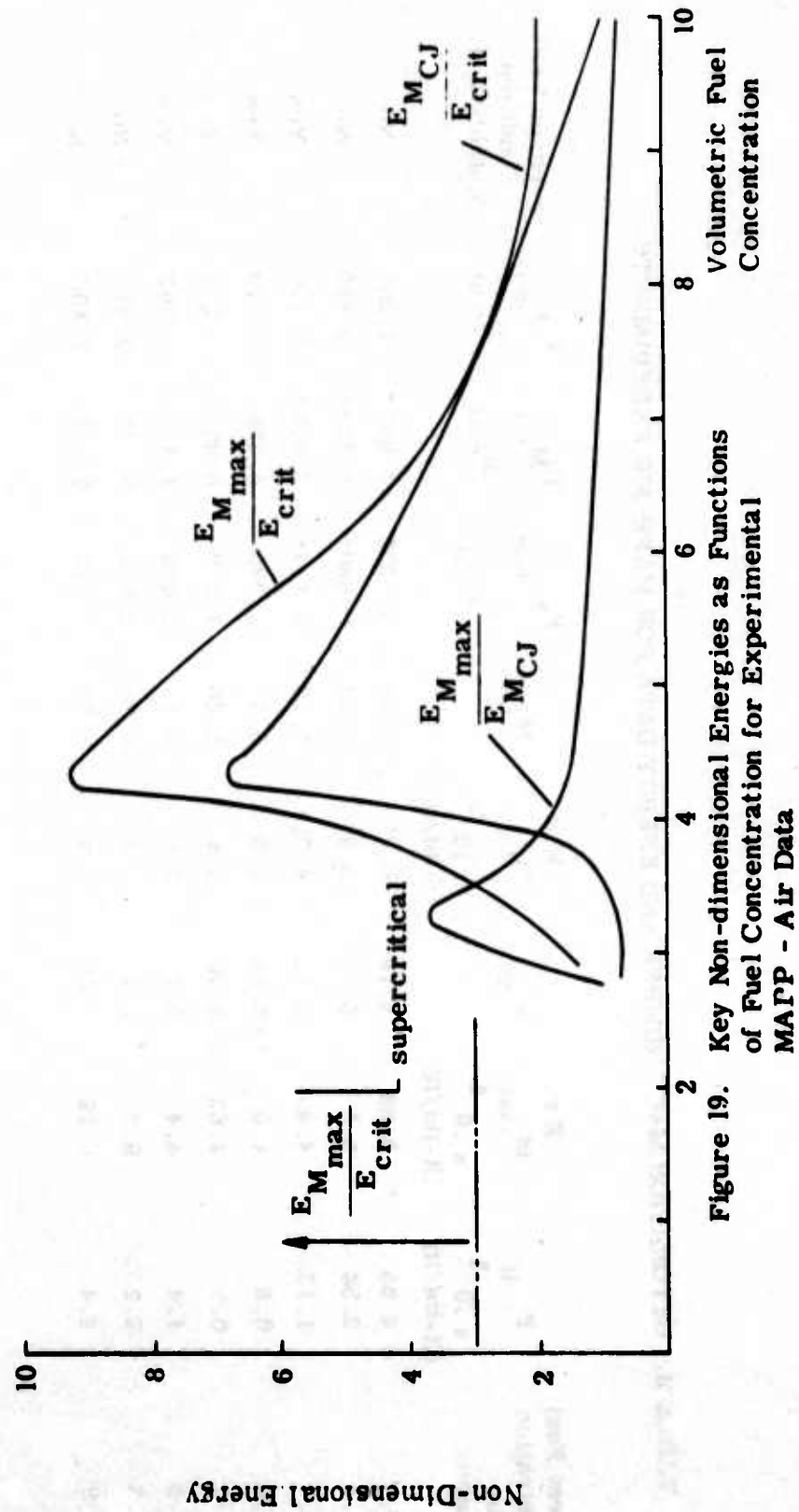
Figure 19. Key Non-dimensional Energies as Functions of Fuel Concentration for Experimental MAPP - Air Data

64

The existence of a definite energy regime wherein supercritical wave propagation was experimentally observed is easily seen. It is of interest to examine this line of thought in light of MAPP-air, as well as available two-phase detonation Mach number data. Plotted in Figure 20 is detonation wave Mach number against volumetric fuel concentration for curves of constant blast source energy. The solid lines represent experimental MAPP-air data, with available kerosene-air two-phase data superimposed. Also given is a curve of M_{CJ} for MAPP-air with the corresponding data given for kerosene-air. A line of E_{crit} may be constructed by the intersection of the appropriate curve of constant E with the appropriate fuel concentration. Hence, the line of E_{crit} for MAPP-air data is shown, again with the corresponding kerosene-air point also shown. The importance of this figure is revealed when it is observed that for the MAPP concentrations which experienced $M_{exp} \geq M_{CJ}$ their non-dimensional energies were $2.8 \leq E/E_{crit} \leq 9.3$. Correspondingly, at the given kerosene concentration M_{exp} was nearly equivalent to M_{CJ} with $E/E_{crit} \sim 2.5$. It is thus apparent that for E/E_{crit} approximately greater than 3.0, wave propagation characteristics associated with the super-critical energy regime can be established and studied. The interval $1.0 < E/E_{crit} < 3.0$ then approximately specifies the critical energy regime, which does indeed seem to be very narrow. This discussion appears to break down as the fuel detonability limits are approached, as shown in Figure 20. In lean mixtures nearly all non-dimensional energies suggest supercritical wave behavior.
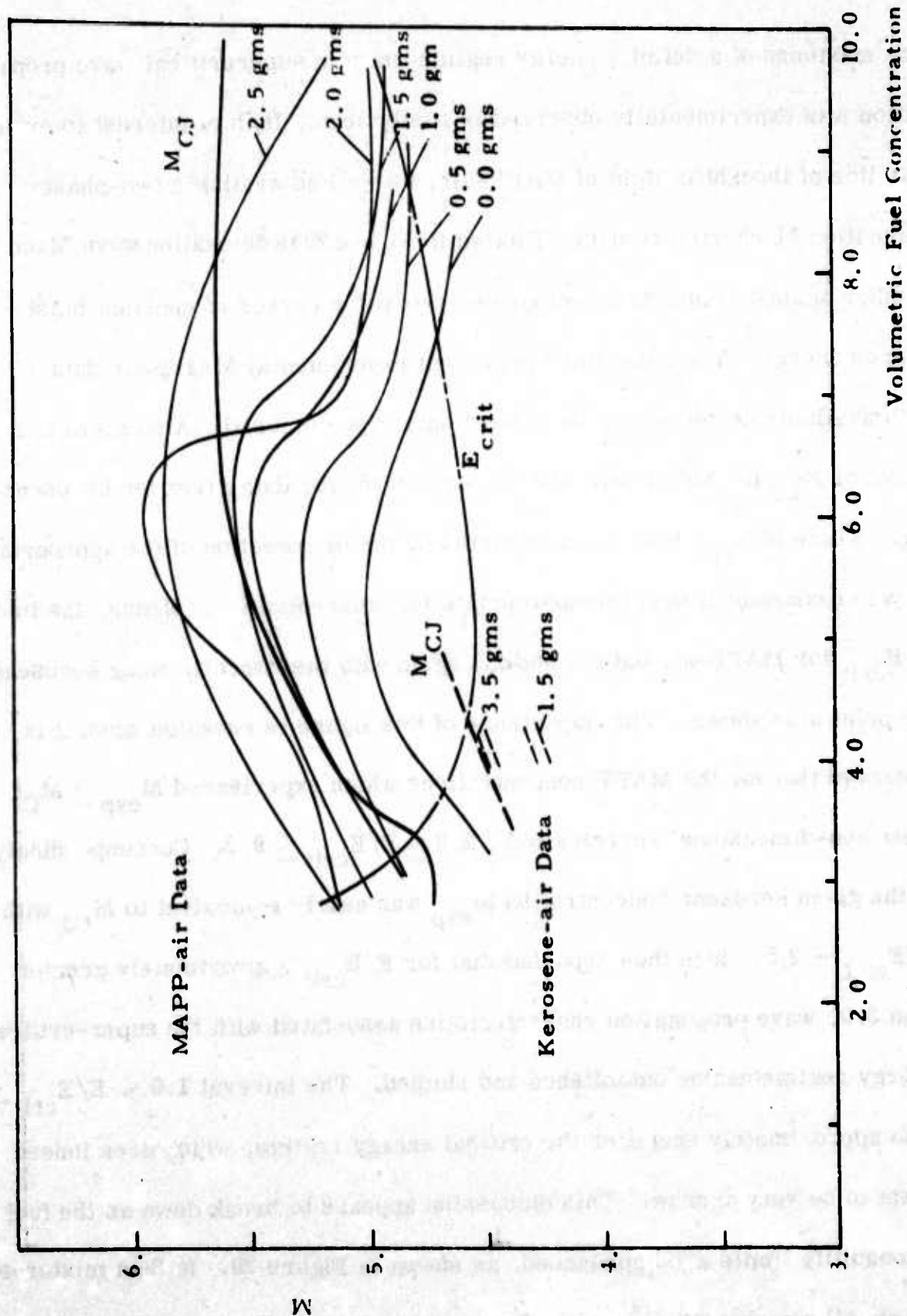
Figure 20. Comparison of Experimental Mach Number Behavior with Theory Plotted Against Fuel Concentration with Varying Blast Source Energy.

This is presumably due to incomplete chemical reactions as the detonation limits are approached, which is easily responsible for M_{exp} deviating from M_{CJ}. The overall detonation wave speed behavior observed in MAPP-air experiments is seen in Figure 21. Plotted is the range of experimental Mach numbers, M_{exp}, obtained. As was already pointed out in the previous discussions, this range is indeed not to be interpreted as a range for experimental error, but rather a function range within which

$$M = M(E) \tag{58}$$

It is foreseen that through the use of spark schlieren data, wave structure may be analyzed as source energy is varied throughout the multiple energy regimes. Perhaps then a more precise estimate of non-dimensional energy intervals may be established.

Experimental transition distances when non-dimensionalized by explosion length, where

$$r_*/r_0 = 2/M_D \, (\gamma_2^2 - 1)^{1/2} \tag{59}$$

for cylindrical wave behavior, compare favorably with those computed based upon theoretical detonation Mach number. Figure 22 is a plot of non-dimensional critical radius against fuel concentration with experimental MAPP-air data superimposed. Also shown is the available kerosene-air data for comparison, with attendant uncertainty displayed in all data.

67
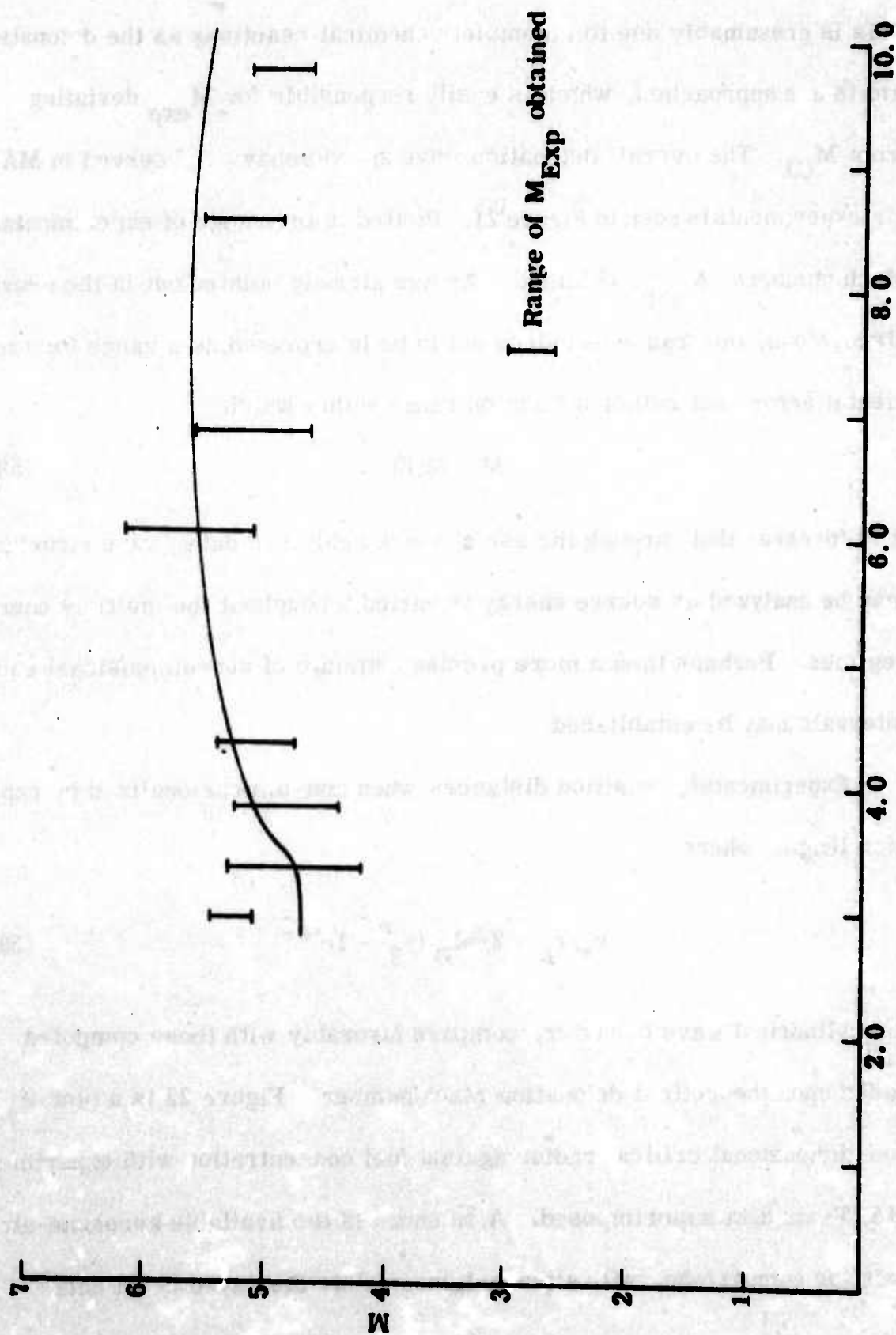
Figure 21. M_{Exp} and M_{CJ} as Functions of MAPP Concentrations.

Some deviation between experiment and theory is expected in view of the observation that exact CJ detonation is usually not attained. Further, even the idealized theory of strong blast wave behavior up to r_* and CJ detonation beyond r_* does not predict the attainment of the CJ Mach number exactly at r_*.

Wave pressure histories at discrete radial locations have also been determined experimentally. Shown in Figure 23 are typical pressure histories at $r = 19.5$ inches and $r = 30.0$ inches for strong blast waves and gaseous and two-phase detonations, at two source energies. Similar volumetric fuel concentrations were chosen for this comparison with 4.3 percent MAPP for the gaseous detonation data, and 4.1 percent kerosene for the two-phase detonation data. The higher source energy initiated a detonation in both of these cases, while the lower energy did not. Examination of such data clearly displays several fundamental features: (1) identifiable difference between pressure levels of detonating and non-detonating cases, (due to wave instabilities this difference is not as distinctive at E_{crit}); (2) higher sustained pressure for gas phase over two-phase detonation; (3) approximate location of transition distance is identifiable in the traces;
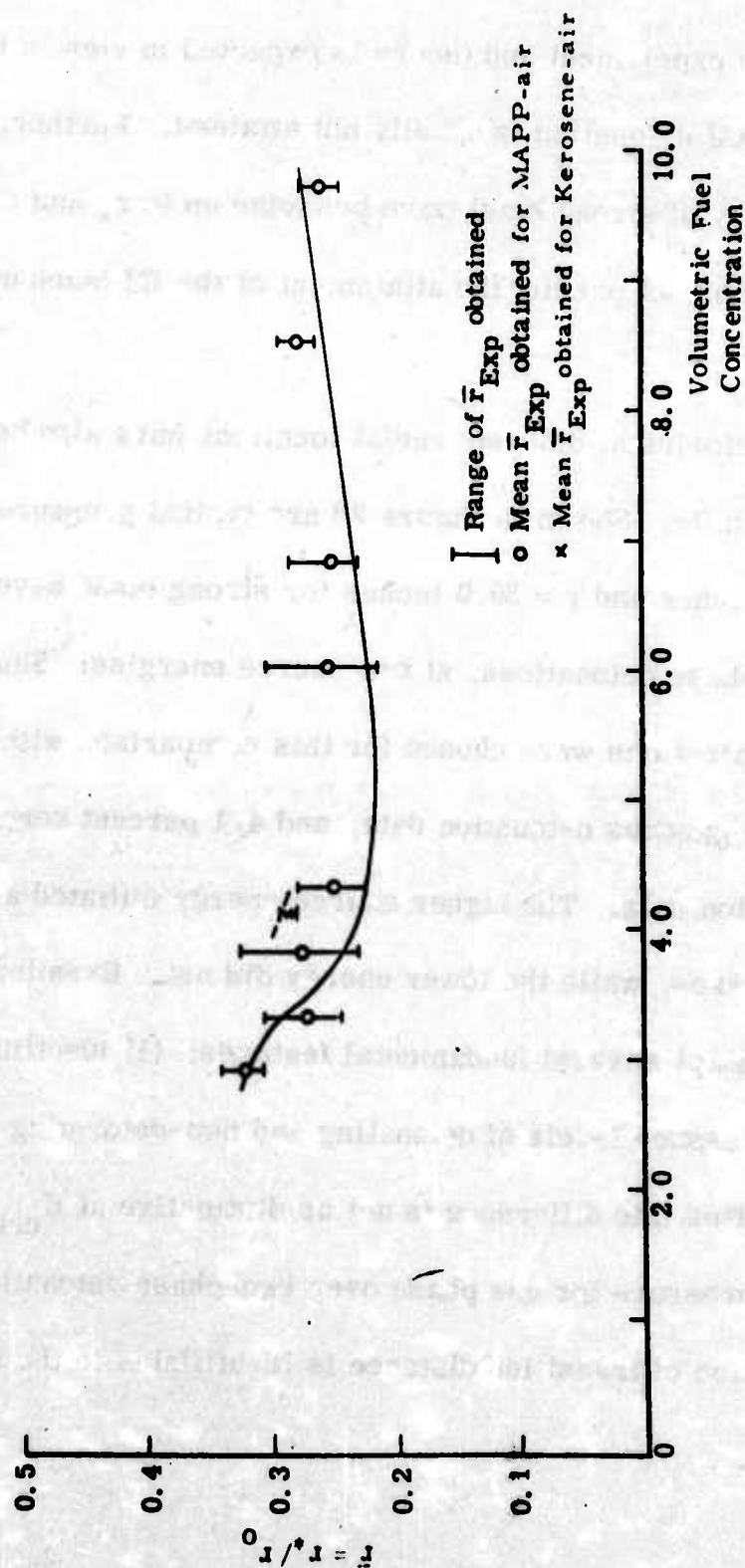
Figure 22. Comparison of Non-Dimensional Detonation Transition Distances with Theoretical Critical Radii for Varying Fuel Concentration.

70
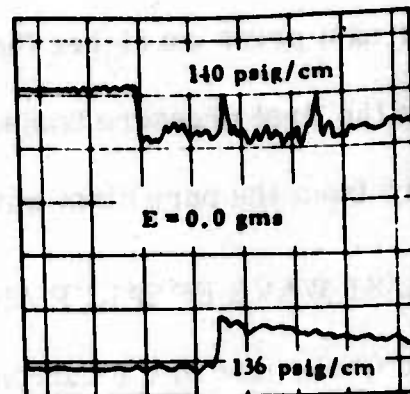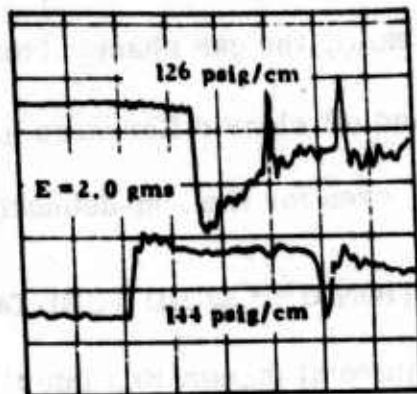
a. Blast Wave Data
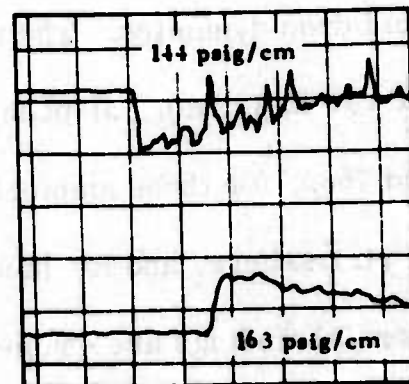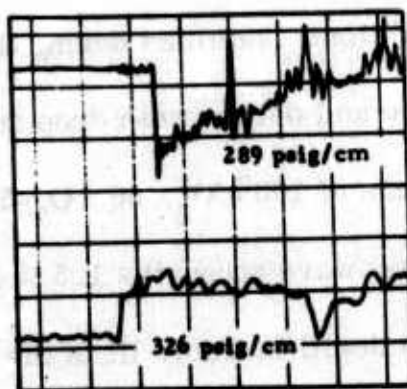
b. Gas-Phase Detonation Data
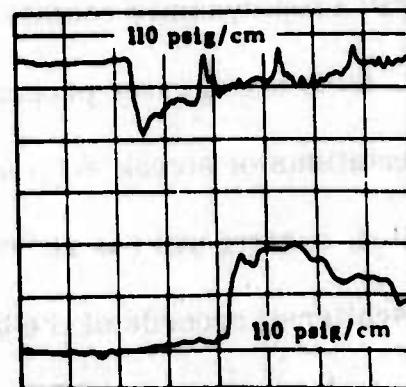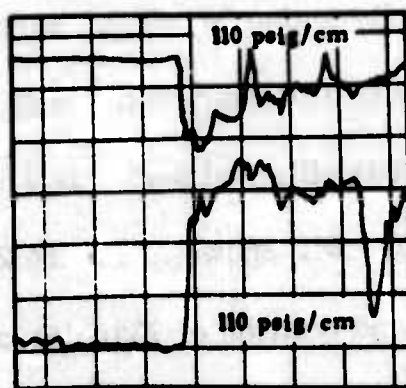
c. Two-Phase Detonation Data

Figure 23. Typical Wave Pressure Histories at Radial Distances of R = 19.5 and R = 30.0 Inches for Blast Source Energies of 2.0 Grams and 0.0 Grams Detasheet. (Upper Traces are for R = 19.5, 50 μsec/cm, Lower Traces are for R = 30.0 Inches, 20 μsec/cm.)

whereas the two-phase mixture detonated between the pressure transducers (downstream pressure higher than upstream), the gas phase mixture detonated prior to the first pressure transducer; and (4) clear differences in pressure from the pure blast wave case, even for the non-detonating cases.

C. BLAST WAVE BREAKUP AND IGNITION OF LIQUID FUEL DROPS

The final phase of the current experimental exploration into the fundamentals of blast initiation of an unconfined fuel-cloud involves the study of individual drop dynamics. The test conditions examined during this phase included two fuels, normal-propyl nitrate and decane with drop sizes of 384μ and 768μ, for three ambient oxidizers of 100% O_2, 50% O_2-50% N_2 and air at 1 atmosphere, and for incident blast wave strengths $1.5 < M < 6$. The essential findings are enumerated in detail in Table III in the form of essential test conditions, drop breakup, stripping, and ignition data, as well as overall drop dynamic conditions initially and at breakup. Such data was obtained from a computer program developed to analyze in detail, digitized representations of streak schlieren records obtained during test runs. The optical system used is shown in Figure 24. Shown in Figure 25 are typical streak schlieren records of the breakup and ignition of 768μ drops of n-propyl nitrate in air and 100% O_2 at standard conditions, for two different source energies. In the records the time axis is running horizontally, for a right running shock, with the distance axis running from bottom to top. The three horizontal lines are reference wires at 1 inch intervals, with which

72

TABLE III. EXPERIMENTAL RESULTS OF INDIVIDUAL DROP DYNAMICS STUDY.

Run Number	Fuel	Drop Diameter D_0 (μm)	Oxidizer	Energy (μJ)	M_{s_1}	$M_{s,s,M}$	t_s (μsec)	V_s/D_0 (mm/μs)	t_b (in.)	t_b (in.)	t_b (μsec)	u_s/D_0 (mm/in.)	T_{sb}	x_{sb} (in.)	$\bar{z}_{sb}$ (μsec)	t_{if} (μsec)	s_{if} (in.)	t (psi)	R_1 $\times 10^{-5}$	W_1 $\times 10^{-5}$	T_{s_1} O_m	t (psi)	R_0 $\times 10^{-5}$	W_0 $\times 10^{-1}$	q_s/q_0	R_0/R_1
2	Propyl Nitrate	768	Air	0.00	3.106	3.108	101.58	4.35	3.079	0.45	14.841	8.565	0.318	0.374	0.094	0.704	...	...	46.39	.3243	.0528	660.4	25.759	.1671	.2976	.5555	.7153
3				0.50	3.127	3.310	107.54	4.12	4.641	0.57	18.975	8.006	0.361	0.409	0.006	0.197	...	...	55.96	.3606	.0617	920.2	18.62	.1395	.3078	.3306	.5603
4				0.50	3.166	3.308		3.59	1.330	0.19	6.336	6.104	0.301	0.399	0.0	0.0	...	...	43.70	.3456	.0604	874.3	6.008	.0902	.1048	.3304	.5465
5				1.00	2.765	2.770	86.64	3.78	4.001	0.48	13.677	8.714	0.347	0.317	0.005	0.0	...	...	146.1	.2438	.0373	1300.	104.9	.2922	.9137	.7145	.6475
6				0.90	2.994	2.990		3.13	3.821	0.48	13.828	11.801	0.047	0.152	0.005	0.177	...	...	153.5	.3421	.0640	1205.	89.66	.2842	.7721	.1505	.4779
7				1.00	3.170	3.000	91.85	1.94	1.074	0.18	4.594	1.385	0.048	0.120	0.003	0.068	74.72	0.49	180.0	.3655	.0686	1552.	11.08	.1505	.0034	.1082	.7611
8				1.50	3.000	3.000		1.94	3.001	0.58	13.501	1.382	0.059	0.130	0.005	0.0	...	...	228.0	.4183	.164	1652.	77.01	.2379	.6034	.3326	.5351
9				3.30	4.598	4.599	46.91	1.34	3.981	0.58	13.591	19.028	0.059	1.431	0.0	0.0	...	...	216.9	.4054	.1794	1662.	154.9	.3224	.6538	.8908	.5669
15				3.30	4.395	4.481	80.36	3.56	6.431	0.67	22.044	8.373	0.277	1.011	0.0	0.0	...	...	602.1	.6103	.3060	2477.	396.0	.4307	1.585	.4753	.6082
22	Propyl Nitrate	768	50% O_2 50% N_2	1.50	3.375	3.374	54.65	1.81	4.138	0.53	17.431	6.891	0.229	0.505	0.0	0.0	41.96	0.45	253.0	.4163	.1595	1564.	257.5	.419	1.978	1.0399	1.0199
33				1.00	3.061	3.061	43.30	1.43	1.701	0.21	6.081	6.632			0.0	0.0	32.33	0.11	184.9	.3971	.1130	1389.	69.67	.2354	.5726	.3707	.6136
34	Propyl Nitrate	768	O_2	3.00	3.304	3.623	45.81	1.51	3.408	0.43	14.303	3.673	0.131	0.295	0.0	0.0	45.18	0.00	237.3	.4647	.1847	1544.	264.2	.4371	2.037	1.0553	1.0325
35				1.75	3.405	3.405	65.81	1.63	3.653	0.31	10.383	4.507	0.140	0.300	0.0	0.001	43.81	0.27	387.3	.4368	.1515	1660.	206.1	.4511	2.297	1.0600	.0335
37				1.00	3.778	3.778	63.87	3.06	3.934	0.43	14.777	5.310	0.175	0.634	0.001	0.039			350.8	.3784	.2581	1685.	175.3	.3540	1.258	.4973	.0661
10	Propyl Nitrate	768	O_2	0.50	2.991	2.784	80.66	2.07	4.397	0.59	19.513	25.119	0.831	1.666	0.043	1.437	**	0.30	309.1	.3811	.1709	1612.	152.5	.3134	1.090	.6585	.7991
11				1.00	3.575	3.105	53.13	1.94	3.913	0.28	9.340	7.251	0.240	0.753	0.015	0.492	44.96	0.13	390.1	.4653	.3871	1810.	242.5	.3887	1.774	.6670	.511
17				1.50	3.401	3.606	58.71	1.04	3.940	0.30	6.760					52.73	0.13	371.3	.4913	.3611	1844.	371.3	.3581	1.487	.5431	.25
18				0.975		3.197	34.07	1.13	2.500	0.71	7.658	6.654	0.230	0.507	0.0	0.003	59.82	0.31	401.4	.5070	.2887	1917.	261.6	.4093	1.009	.7047	.8874
19				0.975	2.949	3.166	64.08	2.12	2.940	0.35	11.500	6.654							198.6	.3824	.1646	1386.	62.26	.3554	.7877	.4438	.6642
21				0.90	3.303	3.321	94.83	1.81	2.854	0.22	7.193	4.955	0.164	0.497	0.0	0.0	61.81	0.48	28.9	.4400	.3180	1803.	119.3	.3856	.9100	.4313	.5491
64	Propyl Nitrate	384	50% O_2 50% N_2	0.00	1.901	1.901	110.13	7.88	6.069	0.46	30.280	9.112	0.603	0.747	0.009	0.579	**	**	33.54	.0983	.0309	851.0	39.14	.0888	.1818	.8889	.9322
65				1.00	3.319	3.319			6.069																		
66				0.50	3.788	3.788	53.45	3.54	6.413	0.31	20.563	9.451	0.625	1.863	0.0	0.0	34.57	0.15	148.2	.1866	.0641	1378.	117.3	.1600	.5073	.7840	.654
67				0.50	3.000	3.786	38.04	2.52	5.037	0.21	13.582	13.582					34.76	0.15	206.2	.1916	.0888	1456.	181.6	.1606	.5480	.6327	.7891
68				1.50	3.582	3.560											25.56	0.12	316.2	.1259	.1181	1770.	196.3	.1791	.7233		
28	Propyl Nitrate	384	O_2	0.50	2.754	2.789	53.50	3.54	7.506	0.43	28.192	6.183	0.409	0.949	0.0	0.0	57.13	0.66	159.0	.1759	.0691	1370.	231.0	.3075	.9603	1.3905	1.1792
29				1.50	3.480	3.400	28.55	1.89	4.616	0.29	19.409	2.307	0.153	0.410	0.0	0.0	33.56	0.50	328.6	.3338	.1210	1721.	282.9	.3211	1.091	.8843	.435
30				1.00	3.515	3.515	64.65	4.28	9.622	0.31	20.683	4.408	0.293	0.836	0.0	0.0	69.15	0.51	325.8	.3338	.1309	1716.	256.2	.3076	.9417	.7935	.6919
31				2.00	3.521	3.521																					
32				3.50	3.500	3.500																					
33				1.25	3.497	3.500	36.37	2.40	5.623	0.39	18.904							...	...	335.6	.2357	.1360	1748.	309.9	.3114	.9968	.8040	.8947
13	Propyl	768	N_2	0.50	2.781	2.811	65.32	2.16	1.767	0.22	7.229	10.844	0.359	0.691	0.005	0.151			149.9	.3529	.1293	1580.	33.86	.1052	.2632	.3192	.4442
1				0.0		2.198																					

TABLE III. EXPERIMENTAL RESULTS OF INDIVIDUAL DROP DYNAMICS STUDY (Concluded).

Figure 24. Streak Schlieren Optical System

75

Figure 25a. Typical Streak Schlieren Record of 768μ Drops of n-Propyl Nitrate, Incident Mach Number of 2.0 in Air.

Figure 25b. Typical Streak Schlieren Record of 768μ Drops of n-Propyl Nitrate, Incident Mach Number of 3.5 in O_2.

a nominal time of 50 μsec along the horizontal can be associated. The fuel drop enters the field of view from the left, it is impacted by the shock entering from the bottom, the drop is subsequently accelerated in the downstream direction, simultaneously shattered and, provided proper conditions exist, ignited. These photographs clearly display the changing local dynamic conditions the drop experiences during its breakup and ignition history. The source energy of Figure 25b was sufficient to cause ignition. In this case the observed ignition time is approximately 45 μsec for an incident Mach number of 3.5. This value is substantially higher than similar data reported by Lu and Slagg[18]. Presumably, this difference is due to the trailing rarefaction associated with the blast wave and the attendant reduction in gas pressure and temperature. This work is unique with regard to this key point, since all previous drop breakup and ignition studies were confined to the simple case of an incident plane shock wave, with which, during the testing interval, no such reductions are associated. A measure of the magnitude of reduction in local drop dynamic conditions is given by the ratios q_b/q_i and Re_b/Re_i, which compare the dynamic pressure and Reynold's number for the drop initial- and breakup-conditions. The data tends to suggest that in general this reduction is quite severe, with typically

$$0.1\, q_i \leq q_b \leq 0.7\, q_i \quad .$$

77

A final reference to Figure 25b will reveal the presence of combustion products carried by the convective gas flow a distance of approximately 65 μs (at the drop location) behind the incident shock. These products originate at the blast source and serve to point out the important difference between explosive/ignitor and spark discharge or even exploding wire blast wave energy sources. This difference of course being the addition of mass to the flowing system upon generation of the blast wave. Practical experimental considerations led to the observation that for too high a blast source energy (approximately 2.5 grams of Detasheet®), all details of the combustion process were literally obscured from view. Some courses of action remain open for possible alleviation of this problem if further tests are warranted. Further detailed analyses of the data reported herein are planned.

REFERENCES

1. Nicholls, J.A., Sichel, M., Fry, R., and Glass, D.R., "Theoretical and Experimental Study of Cylindrical Shock and Heterogeneous Detonation Waves," Fourth International Colloquium on Gasdynamics of Explosions and Reactive Systems, San Diego, California, 10-13 July 1973.

2. Lee, J.H., "Gasdynamics of Detonations," Astronautica Acta, 17, 1972, 455-466.

3. Chernyi, G.G., Korobeinikov, V.P., Levin, V.A., and Medvedev, S.A., "One-Dimensional Unsteady Motion of Combustible Gas Mixtures Associated with Detonation Waves," Astronautica Acta, 15, 1970, 259-266.

4. Korobeinikov, V.P., "Gas-Dynamics of Explosions," Annual Review of Fluid Mechanics, 3, 1971, 317-346.

5. Sedov, L.I., Similarity and Dimensional Methods in Mechanics, Academic Press, New York, 1959.

6. Taylor, G.I., "The Formation of a Blast Wave by a Very Intense Explosion," Proc. Roy. Soc., Ser. A., 201, 1950, 159-174.

7. Gordon, S. and McBride, B., "Computer Program for Calculation of Complex Chemical Equilibrium Compositions, Rocket Performance, Incident and Reflected Shocks, and Chapman-Jouguet Detonations," NASA SP 273, 1971.

8. Nicholls, J.A., Fry, R.S., Glass, D.R., Sichel, M., VanderSchaaf, J., and Sternstein, A.J., "Fundamental Aspects of Unconfined Explosions," Tech. Rept. AFATL-TR-72-39, AF Armament Lab., Eglin AFB, Fla., March 1972.

9. Nicholls, J.A., Sichel, M., Fry, R.S., Hu, C., Glass, D.R., DeSaro, R., and Kearney, K., "Fundamental Aspects of Unconfined Explosions," Tech. Rept. AFATL-TR-73-125, AF Armament Lab., Eglin AFB, Fla., March 1973.

10.   Taylor, G. I., "Gas Dynamics of Combustion and Detonation,"
        Sec. G. in Fundamentals of Gas Dynamics, Vol. III, Princeton
        Ser. in High Speed Aerodynamics and Jet Propulsion (H. Emmons,
        ed.), Princeton University Press, 1958.

11.   Brode, H. L., Glass, I. I., and Oppenheim, H. K., "Gas Dynamics
        of Explosions Today," Shock Tube Research Proc. of the Eighth
        Intl. Shock Tube Symp., Imperial College, London (Stollery, J. L.,
        ed.), 5-8 July 1971.

12.   Sichel, M., "A Hydrodynamic Theory for the Propagation of
        Gaseous Detonations through Charges of Finite Width," AIAA J.,
        4, 1966, 264-272.

13.   Dabora, E. K., Nicholls, J. A., and Morrison, R. B., "The
        Influence of the Compressible Boundary on the Propagation of
        Gaseous Detonations," Tenth Symposium (International) on
        Combustion, The Combustion Institute, Pittsburgh, Pa., 1965, 817.

14.   Sommers, W. P., Morrison, R. B., "Simulation of Condensed
        Explosive Detonation Phenomena with Gases," Phys. Fluids, 5,
        1962, 241-248.

15.   Liepmann, H. W. and Roshko, A., Elements of Gasdynamics,
        John Wiley and Sons, Inc., New York, 1957.

16.   Fry, R. S. and Nicholls, J. A., "Blast Initiation and Propagation of
        Cylindrical Detonations in MAPP-Air Mixtures," presented at the
        AIAA 12th Aerospace Sciences Meeting, January 30-February 1,
        1974, Washington, D. C., Preprint No. 74-149, accepted for publi-
        cation in the AIAA J.

17.   Bach, G. G., Knystautas, R. and Lee, J. H., "Initiation Criteria
        for Diverging Gaseous Detonations," 13th Symposium (International)
        on Combustion, The Combustion Institute, Pittsburgh, Pa., 1971,
        1097-1110.

18.   Lu, P. -L. and Slagg, N., "Chemical Aspects in the Shock Initiation
        of Fuel Droplets," Astronautica Acta, 17, 1972, 693-720.

DOCUMENT CONTROL DATA - R & D

(Security classification of title, body of abstract and indexing annotation must be entered when the overall report is classified)

1 ORIGINATING ACTIVITY (Corporate author)	2a. REPORT SECURITY CLASSIFICATION
The University of Michigan Ann Arbor, Michigan 48105	UNCLASSIFIED
	2b. GROUP

3 REPORT TITLE

FUNDAMENTAL ASPECTS OF UNCONFINED EXPLOSIONS

4 DESCRIPTIVE NOTES (Type of report and inclusive dates)

Final Report - 22 January 1973 to 2 February 1974

5 AUTHOR(S) (First name, middle initial, last name)

J. A. Nicholls   R. S. Fry   R. DeSaro
M. Sichel   C. Hu   K. Kearney

6 REPORT DATE	7a. TOTAL NO. OF PAGES	7b. NO. OF REFS
August 1974	96	18

8a. CONTRACT OR GRANT NO.	9a. ORIGINATOR'S REPORT NUMBER(S)
F08635-71-C-0083	
b. PROJECT NO. 2513	
c. Task No. 07	9b. OTHER REPORT NO(S) (Any other numbers that may be assigned this report)
d. Work Unit No. 001	AFATL-TR-74-123

10. DISTRIBUTION STATEMENT

Distribution limited to U. S. Government agencies only; this report documents test and evaluation; distribution limitation applied **August 1974**. Other requests for this document must be referred to the Air Force Armament Laboratory (DLJ), Eglin Air Force Base, Florida 32542.

11 SUPPLEMENTARY NOTES	12. SPONSORING MILITARY ACTIVITY
Available in DDC	Air Force Armament Laboratory Air Force Systems Command Eglin Air Force Base, Florida 32542

13. ABSTRACT

Blast wave initiation of detonation in a completely homogeneous cloud is considered. The self similar character of strong blast waves and Chapman-Jouguet detonation waves is used to arrive at simplified closed form solutions for the generation of ground impulse and dynamic impulse, up to the time that the detonation arrives at the edge of the cloud. The dependence of impulse on fuel properties and cloud geometry is predicted. The influence of side relief at the top of the cloud is considered. Experimental studies are described which investigate the initiation, transition, and quasi-steady propagation processes associated with blast initiated, cylindrical detonation waves. Experiments were conducted with all gaseous and heterogeneous fuel-air mixtures wherein a specially designed sectored shock tube was employed. A complete volumetric range of MAPP (methyl acetylene, propane, propadiene)-air mixtures was investigated. Some results on the breakup and ignition of single fuel drops, when subjected to strong blast waves, are presented.

DD FORM 1473
1 NOV 65

14. KEY WORDS	LINK A		LINK B		LINK C	
	ROLE	WT	ROLE	WT	ROLE	WT
Fuel-Air Explosive Combustible Cloud Chapman-Jouguet Detonation Waves						

END - 2 - 75